The XXL survey XV: evidence for dry merger driven BCG growth in XXL-100-GC X-ray clusters

S. Lavoie,[1][★] J. P. Willis,[1][★] J. Démoclès,[2] D. Eckert,[3] F. Gastaldello,[4] G. P. Smith,[5]
C. Lidman,[6] C. Adami,[7] F. Pacaud,[8] M. Pierre,[2][★] N. Clerc,[9] P. Giles,[10] M. Lieu,[5]
L. Chiappetti,[4] B. Altieri,[11] F. Ardila,[12] I. Baldry,[13] A. Bongiorno,[14] S. Desai,[15]
A. Elyiv,[16,17] L. Faccioli,[2] B. Gardner,[6,18] B. Garilli,[4] M. W. Groote,[19]
L. Guennou,[4,20] L. Guzzo,[21] A. M. Hopkins,[6] J. Liske,[22] S. McGee,[5]
O. Melnyk,[23,24] M. S. Owers,[6,18] B. Poggianti,[25] T. J. Ponman,[5]
M. Scodeggio,[4] L. Spitler[6,18] and R. J. Tuffs[19]

Affiliations are listed at the end of the paper

ABSTRACT

The growth of brightest cluster galaxies (BCGs) is closely related to the properties of their host cluster. We present evidence for dry mergers as the dominant source of BCG mass growth at $z \lesssim 1$ in the XXL 100 brightest cluster sample. We use the global red sequence, Hα emission and mean star formation history to show that BCGs in the sample possess star formation levels comparable to field ellipticals of similar stellar mass and redshift. XXL 100 brightest clusters are less massive on average than those in other X-ray selected samples such as LoCuSS or HIFLUGCS. Few clusters in the sample display high central gas concentration, rendering inefficient the growth of BCGs via star formation resulting from the accretion of cool gas. Using measures of the relaxation state of their host clusters, we show that BCGs grow as relaxation proceeds. We find that the BCG stellar mass corresponds to a relatively constant fraction 1 per cent of the total cluster mass in relaxed systems. We also show that, following a cluster scale merger event, the BCG stellar mass lags behind the expected value from the M_{cluster}–M_{BCG} relation but subsequently accretes stellar mass via dry mergers as the BCG and cluster evolve towards a relaxed state.

Key words: galaxies: clusters: general – galaxies: elliptical and lenticular, cD – galaxies: evolution – galaxies: interactions – X-rays: galaxies: clusters.

1 INTRODUCTION

Due to their dominance and location near the centre of clusters, brightest cluster galaxy (BCG) evolution is of great interest. In the current paradigm, BCGs are formed hierarchically by mergers with other cluster members. Observations of $z \lesssim 0.1$ BCGs have shown that they follow a steeper size–luminosity scaling relation than other early-type galaxies. For their luminosity, BCGs are larger than expected from the bulk of early-type galaxies, indicating that dissipationless mergers play an important role in their formation (e.g. Bernardi et al. 2007; Liu et al. 2008). Around $z \sim 1$, BCGs gain their *identity* as they unambiguously emerge as the dominant galaxy within a cluster (De Lucia et al. 2006). Although early theoretical (e.g. Merritt 1984; Merritt 1985; Schombert 1987) and more recent

observational work (Collins et al. 2009; Stott et al. 2010) favour a scenario where BCGs were almost entirely assembled at $z \sim 1$, work by McIntosh et al. (2008), Liu et al. (2009) and Edwards & Patton (2012) indicate that BCGs are still growing at the present epoch. Other work by Lidman et al. (2012), Burke & Collins (2013) and Liu et al. (2015) indicate that BCGs at $z < 1$ still undergo major merger events and grow by a factor of $\sim$2 from $z \sim 1$ to the present epoch. Simulations have shown that most of the mass probably comes from a small ($\lesssim 10$) number of merging events (De Lucia & Blaizot 2007, Ruszkowski & Springel 2009). Observation of mass segregation in clusters (Dressler et al. 1997; Adami, Biviano & Mazure 1998; Biviano et al. 2002; Lidman et al. 2013) and the presence of multiple bound companions around BCGs (Burke & Collins 2013) show that clusters and the BCG environment are dynamically evolving in a way that readily makes stellar material available to BCGs.

BCG evolution is intimately linked to the host cluster evolution as BCG growth requires an influx of material from the cluster. There

★ E-mail: slavoie@uvic.ca (SL); jwillis@uvic.ca (JPW); marguerite.pierre@cea.fr (MP)

are two possible growth channels for BCGs: the accretion of stars via gas-poor, or dry, mergers and the formation of new stars *in situ* from accreted gas brought to the BCG by cooling flows or from a gas-rich, or wet, merger event. Mass growth via dry mergers can only be a major contributor to BCG mass evolution if kinematic processes in the cluster such as dynamical friction (Chandrasekhar 1943) make that mass available for accretion on to the BCG in time-scales less than the Hubble time. Fabian (2012) reports that most of the UV and IR luminosity of BCGs in cool-core clusters seem to come from vigorous *in situ* star formation, presumably fuelled by residual cooling flows. BCG growth via such *in situ* star formation requires the host cluster to exist in a relaxed or undisturbed state as the formation of cooling flows could be easily disrupted by cluster merging events (e.g. Ricker & Sarazin 2001).

Feedback from a central active galactic nucleus (AGN) can also disrupt cooling flows via the injection of energy into the intracluster medium (ICM). The duty cycle of radio-mode feedback can be more than 60 per cent, suppressing the amount of gas actually reaching the BCG (e.g. Bîrzan et al. 2012). Star formation resulting from cooling flows also requires a BCG to be situated close to the centroid of the X-ray emission in clusters for the gas to actually be accreted (Edwards et al. 2007; Bildfell et al. 2008; Rafferty, McNamara & Nulsen 2008).

Recent work also indicate that BCGs dominant growth source changes around $z \sim 1$. Webb et al. (2015) show that very IR-luminous BCGs are only found at $z > 1$ and McDonald et al. (2016) find that star formation in BCGs is more significant at $z > 1$, even in dynamically disturbed clusters. Both papers, in addition to work done by Vulcani et al. (2016) and Liu et al. (2013) indicate that *in situ* star formation seems to dominate stellar mass growth at $z \gtrsim 1$ before being replaced by dry mergers at $z \lesssim 1$. Determining the source of BCG mass growth provides not only a direct indication of its own evolution but also of the history of its cluster environment.

To understand the relationship between BCGs and their host clusters requires a large sample of such systems, ideally drawn from a range of cluster mass and redshift, and selected according to a simple set of physical criteria. In this paper we investigate the properties of a large sample of clusters and BCGs drawn from the XXL survey. At more than 6 Ms total exposure time over two 25 deg^2 fields, XXL is the largest *XMM–Newton* programme to date (Pierre et al. 2016, hereafter XXL Paper I). The two XXL survey fields are referred to as XXL-N, centred on the XMM-LSS and CFHTLS W1 field, and XXL-S, centred on the Blanco Cosmology Survey (BCS) field. Each consists of an overlapping mosaic of 10 ks XMM exposures.

The XXL survey offers a unique perspective on the evolution of low-to-intermediate mass X-ray clusters. Clusters and BCGs are not homogeneous, either at fixed mass or redshift. There are considerable variations in their properties which makes necessary the study of a numerically large sample. The large amount of optical, infrared and spectroscopic data available or obtained by XXL makes it possible to study a large and well-defined X-ray cluster sample up to $z \sim 1$. More importantly, it enables us to relate photometric and spectroscopic measures of BCGs to the relaxation state of the clusters. We use the sample of the 100 brightest XXL clusters[1] for our work (XXL-100-GC; Pacaud et al. 2016, hereafter XXL Paper II) and find that the relaxation state of clusters is very powerful tool to help follow and understand BCG growth.

The paper is organized as follows: in Section 2 we describe the 100 brightest clusters sample and the multi-λ data used; in Section 3, we present the BCG selection criteria and final sample; we present the various measurements performed on the sample in Section 4; we discuss our results in Section 5. A WMAP9 cosmology is used unless otherwise stated.

2 XXL-100-GC BRIGHTEST CLUSTERS SAMPLE

2.1 Clusters

Galaxy clusters are identified from processed XMM images in the following manner: source extraction is performed by applying SEXTRACTOR (Bertin & Arnouts 1996) to wavelet-filtered XMM images. Surface photometry is then performed on selected sources using the custom XAMIN pipeline with sources characterized by maximum-likelihood values of `extent`, `extent_likelihood` and `detection_likelihood` (Pacaud et al. 2006). The application of appropriate cuts through this detection parameter space generate respectively the C1 cluster sample, which is uncontaminated by misclassified sources or artefacts (Pacaud et al. 2006; Pacaud et al. 2007; Clerc et al. 2012; Clerc et al. 2014) and the C2 sample which displays 30–50 per cent contamination (Pierre et al. 2006; Adami et al. 2011). The survey cluster selection function is expressed in terms of the surface brightness of model clusters realized within XMM images (Pacaud et al. 2006). A growth curve analysis is used to measure fluxes for the 200 brightest clusters within the XXL survey footprint (Clerc et al. 2012). The analysis employs local background estimation, nearby-source masking and interactive cluster centring. XXL-100-GC clusters are selected from this list with fluxes quoted in a 1 arcmin radius circular aperture. The sample contain 51 clusters located in XXL-N and 49 in XXL-S (XXL Paper II).

Cluster X-ray temperatures for the XXL-100-GC sample are presented in (Giles et al. 2016, hereafter XXL Paper III). X-ray spectra of each cluster were extracted using an aperture of radius 300 kpc with a minimum of five counts per spectral bin in the 0.4–7.0 keV band. Temperatures are not core excised due to the limited PSF of *XMM–Newton* and lie mostly in the 1 KeV $\leq T_{300\,\mathrm{kpc}} < 6$ KeV range.

Cluster weak-lensing masses for the XXL-100-GC sample are presented in Lieu et al. (2016, hereafter XXL Paper IV). Masses are computed from an internal weak-lensing $M - T$ scaling relation. calibrated using a shear profile analysis of 38 XXL-100-GC clusters located within the footprint of the CFHTLenS shear catalogue. Following Miller et al. (2013) and Velander et al. (2014), the authors build a shear profile from the ellipticity analysis of galaxies found to be behind the individual clusters in the CFHTLenS shear catalogue. A Navarro, Frenk and White (NFW; Navarro, Frenk & White 1997) profile is fit to the shear profile and integrated out to $r_{500,\,WL}$[2] to obtain the values of weak-lensing masses $M_{500,\,WL}$ for the clusters. The average $M_{500,\,WL} - T_{300\,\mathrm{kpc}}$ scaling relation is then used to get both $r_{500,\,MT}$ and $M_{500,\,MT}$, the mass within r_{500}, for all XXL-100-GC clusters so that all masses are based on the scaling relation. For the sake of simplicity, we shall use r_{500} and M_{500}, respectively to denote $r_{500,\,MT}$ and $M_{500,\,MT}$.

---

[1] Available on CDS in catalogue IX/49/xxl100gc and via the Master Catalogue Database in Milan at: http://cosmosdb.iasf-milano.inaf.it/XXL/

[2] Defined as the radius within which the average total mass density of a cluster equals 500 times the critical density of the Universe at the cluster redshift as obtained from the weak-lensing analysis
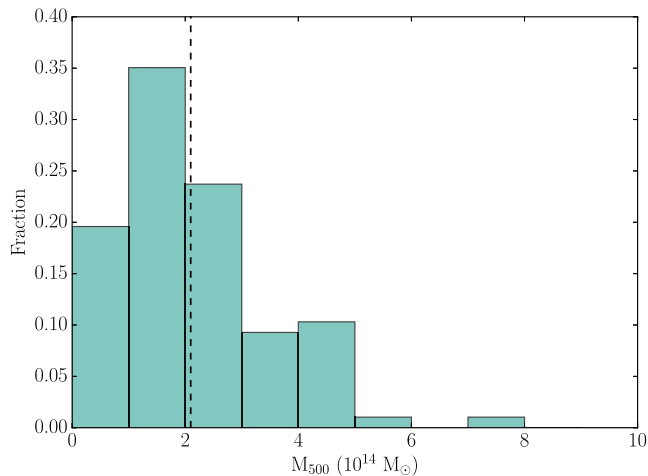
Figure 1. Normalized mass distribution obtained from X-ray scaling relations for XXL-100-GC. The dashed vertical line indicate the average XXL-100-GC cluster mass of just over 2×10^{14} M$_\odot$.

Fig. 1 shows the normalized distributions of cluster masses for XXL-100-GC as obtained from the [XXL Paper IV](#) $M - T$ relation.[3] The average mass within r_{500} of XXL-100-GC clusters is $\sim 2 \times 10^{14}$ M$_\odot$, a value which is generally lower when compared to the average mass of other X-ray cluster samples such as REXCESS ($\sim 3 \times 10^{14}$ M$_\odot$, Haarsma et al. 2010), LoCuSS[4] ($\sim 4 \times 10^{14}$ M$_\odot$, Smith et al., in preparation), CLASH ($\sim 6 \times 10^{14}$ M$_\odot$, Merten et al. 2015) or HIFLUGCS ($\sim 6 \times 10^{14}$ M$_\odot$, Reiprich & Böhringer 2002). Some care must be exercised when comparing XXL-100-GC to samples, not just of differing mass, but also of differing sample selection criteria. In this sense, comparing the properties of XXL-100-GC to an existing, yet lower redshift, flux-limited cluster sample such as HIFLUGCS ($z < 0.1$; Reiprich & Böhringer 2002) is of interest as it reproduces many of the selection biases inherent in flux – as compared to luminosity-based selection.

2.2 Multiwavelength data

XXL has been constructed as a multiwavelength survey and the complete list of XXL-PI and external programmes can be found in Pierre et al. (2016). The present work primarily employs optical and near-infrared photometric data as well as photometric and spectroscopic redshifts. The XXL-N field overlaps the W1 field from CFHTLS wide MegaCam survey (Gwyn 2012). All but five of the XXL-N clusters have *ugriz* photometry from MegaCam with a point-source *i*-band depth of ~ 25 AB. The remaining five clusters are located in a northern extension of the CFHTLS W1 field known as the ABC field and have *grz* MegaCam photometry to the same depth as CFHTLS.

Galaxy magnitudes are taken from the *i*-band selected CFHTLS Wide catalogue (Gwyn 2012).[5] MAG_AUTO magnitudes in the catalogue are computed with SExtractor 2.5.0 using the adaptative aperture described in Bertin & Arnouts (1996). Extensive testing by Bertin & Arnouts has shown that this aperture produces very

consistent results for galaxies of any shape or ellipticity, missing on average 6 per cent of the flux with only 2 per cent variations rms. We correct for the missing flux and combine the variations with photometric errors to obtain consistent final total magnitudes in both CFHTLS and ABC fields.

W1 source photometric redshifts are taken from the latest CFHTLS-T0007 release (Ilbert et al. 2006; Coupon et al. 2009) and have a typical error of $\sigma_{W1} = 0.04$ for $i \leq 22.5$.

Few sources in the ABC field have spectroscopic redshifts. Instead we combine *grz* photometry with the large number of sources with spectroscopic redshifts in the W1 field to train a generalized linear models code in the ABC field (Elliott et al. 2015). The photometric redshifts are found by passing the *grz* photometry to the PYTHON package *CosmoPhotoz*[6] together with the photometry and spectroscopic redshifts of about a thousand sources in W1. This results in photometric redshifts with $\sigma_{ABC} = 0.065$ for sources with $z \leq 23.0$ in the ABC fields.

The XXL-S field is located in the sky area covered by the BCS with *griz* photometry (Desai et al. 2012). Although BCS data is shallower than CFHTLS with a point-source *i*-band depth of 24, the area is also part of the deeper Dark Energy Survey[7] (DES), a 5000 deg^2 field observed with the Dark Energy Camera (DECam; Flaugher et al. 2015) in *grizY*. While the coverage is still incomplete in the *i* band, it is supplemented by deeper XXL-PI observations in the *grz*-band covering the Southern field with a *z*-band depth of ~ 25 (Desai et al., in preparation). DECam photometry is preferred whenever available. BCS magnitudes are taken from the survey catalogues described in Bleem et al. (2015). Similarly, DECam data is taken from the survey catalogues where total magnitudes are computed from PSF corrected model fitting photometry [see Bertin (2011) and Mohr et al. (2012)]. Photometric redshifts for sources in the Southern field are part of the BCS data and were obtained by Menanteau et al. (2010) using the Benítez (2000) BPZ algorithm from BCS *griz* photometry. The typical photometric redshift error is $\sigma_{BCS} = 0.06$ for $i \leq 22.5$.

Spectroscopic redshifts for both XXL-N and XXL-S are drawn from a variety of sources. Targeted spectroscopy of individual clusters has been obtained as part of ESO Large Programme 191.A-0268. Further spectroscopy is available from the VIMOS Public Extragalacic Redshift Survey (VIPERS), a large and deep VIMOS (Le Fèvre et al. 2003) redshift survey focusing on the $0.5 < z < 1.2$ redshift range (Garilli et al. 2014, Guzzo et al. 2014) that partially overlaps with XXL-N. The Galaxy And Mass Assembly (GAMA) survey is another large spectroscopic data set that overlaps XXL-N, contributing low-resolution, high-completeness spectroscopy of galaxies in the XXL-N field to $r < 19.8$ (Hopkins et al. 2012, Baldry et al. 2014, Liske et al. 2015). Data exchange with the VIPERS and GAMA teams has made available thousands of spectroscopic redshifts for this work. In addition, publicly available spectroscopic redshifts from SDSS DR12 (Gunn et al. 2006, Eisenstein et al. 2011, Dawson et al. 2013, Smee et al. 2013, Ahn et al. 2014) and the VIMOS VLT deep survey (Le Fèvre et al. 2005) are used where they overlap with XXL-N. Many smaller XXL programmes were undertaken to complement the spectroscopic redshifts in the Northern and Southern fields by focusing on known XXL clusters. Most of the spectra in the South have been obtained with the AAOmega spectrograph (Saunders et al. 2004; Smith et al. 2004) on the Anglo-Australian Telescope (Lidman et al. 2016).

---

[3] Most colours used in figures in this work were optimized for readability using the *ColorBrewer* tool from www.ColorBrewer.org by Cynthia A. Brewer, Geography, Pennsylvania State University.

[4] http://www.sr.bham.ac.uk/locuss/home.php

[5] http://www.cadc-ccda.hia-iha.nrc-cnrc.gc.ca/en/megapipe/cfhtls/uc.html

[6] http://cosmophotoz.readthedocs.org

[7] http://www.darkenergysurvey.org/survey/des-description.pdf

Table 1. Summary of spectroscopic data covering XXL-100-GC fields used for this work.

Instrument/Programme	Field	Resolution	Coverage	Typical t_{exp}(s)
VIMOS/VIPERS	N	$R=1200$	16 deg^2	2700
VIMOS/VLT deep survey	N	$R=230$	0.61 deg^2	16 200
AAOmega/GAMA	N	$R=1400$	23.5 deg^2 overlap with XXL	3000–5000
BOSS/SDSS DR12	N	$R=1300–3000$	All XXL-N	2700
AF2/XXL-PI	N	$R=1200$	Individual clusters	7200/14 400
EFOSC2/XXL-PI	N+S	$R=300$	Individual clusters	2700
FORS2/XXL-PI	N+S	$R=600$	Individual clusters	2400
AAOmega/XXL-PI	S	$R=1400$	25 deg^2	5000–10 000s

Table 1 lists basic information on the various sources of spectroscopic data.

Since we have access to such a large number of photometric and spectroscopic redshifts in both the North and South field, it is possible to evaluate and correct the *redshift bias*. Due to the inherent difficulty of associating the right template to a galaxy, photometric redshifts can show systematic offset from their spectroscopic counterpart. One has to correct for this effect to reliably associate galaxies with their host cluster. In XXL-100-GC data, this effect is larger at $z_{spec} \lesssim 0.1$ and $z_{spec} \gtrsim 0.8$. Assuming that spectroscopic redshifts are right, we build a redshift bias correction curve for each field from the sources that have both a spectroscopic and photometric redshift. We then apply the correction to all sources that only have a photometric redshift and use those corrected values for this work.

3 BRIGHTEST CLUSTER GALAXIES

Given the availability of good quality multiband photometry together with photometric and spectroscopic redshifts to $z < 1$, a simple set of criteria can be used to identify BCGs. For the present work, we define a BCG as:

(i) the brightest galaxy in z-band,
(ii) within $0.5 \times r_{500}$ of the cluster X-ray centroid,
(iii) with a redshift that is consistent with that of the cluster as determined from all the redshifts available around the X-ray centroid.

A coarse selection of possible cluster members is first done using photometric redshifts. Galaxies within $0.5 \times r_{500}$ of a cluster X-ray centroid are considered possible members if their photometric redshift falls within:

$$|z_{gal} - z_{cl}| \leq \sigma_x \times (1 + z_{cl}),$$

where z_{gal} is the galaxy photometric redshift, z_{cl} is the cluster redshift and σ_x is the 1σ error on the photometric redshift from the method used in the different fields ($\sigma_{W1} = 0.04$ for $i \leq 22.5$, $\sigma_{BCS} = 0.06$ for $i \leq 22.5$ and $\sigma_{ABC} = 0.065$ for $z \leq 23.0$). The brightest z-band galaxy from that selection is used as a candidate BCG. In ~90 per cent of these cases, visual inspection confirms that the selected BCG is a sensible choice. For the remaining ~10 per cent of systems, photometric redshifts are ignored and the BCG candidates are identified from photometry alone before being visually confirmed. Spectroscopic redshifts are available for all but three BCGs and of those with spectra all are confirmed to be <3000 km s^{-1} from their cluster redshift. Additionally, all of the BCGs identified from photometry alone have a spectroscopic redshift consistent with the host cluster.

Some XXL-100-GC clusters are excluded from this study for various reasons. XLSSC 088, XLSSC 092, XLSSC 110, XLSSC 501,

XLSSC 526 and XLSSC 536 are excluded because the photometry of their identified BCG is possibly contaminated by obvious foreground objects along the line of sight. XLSSC 089, XLSSC 094 and XLSSC 102 are excluded due to the lack of redshifts available to confirm selections that are dubious. Two additional clusters, XLSSC 504 and XLSSC 508, are excluded due to possible contamination of their X-ray centroid from an AGN. XLSSC 052 and XLSSC 062 are excluded because they have only been observed by CFH12K in a few bands. Additional clusters are excluded because measurements of their mass or X-ray relaxation are unavailable. Our final sample consists of 85 clusters, 45 of which are in the Northern field and 40 in the Southern field. For the sake of simplicity, XXL-100-GC will refer to those 85 clusters for the remainder of the paper. BCG positions and some of their characteristics determined later in the paper are presented in Table A1.

4 MEASUREMENTS

A range of measurements can be performed upon the sample to search for evidence of a particular source of BCG growth. We describe these in detail in the following sections and summarize them here. The position of the BCG in relation to the X-ray centroid of their host cluster is measured and an estimate of the X-ray emitting gas concentration is taken from Démoclès et al. (in preparation). Both measures are employed as indicators of the relaxation state of the clusters. The quality of the photometry in the W1 field and the size of the BCG sample enable us to determine the average star formation history (SFH) for the BCGs. From this model, we compute stellar masses for all XXL-100-GC BCGs. We use photometric and spectroscopic redshifts to identify individual members of a given cluster and measure the difference in magnitude between the BCG and bright cluster members as well as investigate evidence of luminosity segregation. We employ the results from a semi-analytic simulation of galaxy evolution to obtain an insight into the distribution of galaxy masses accreted by the BCG. Where available, Hα emission line fluxes are measured from SDSS DR12 spectroscopy and are employed to determine the level of ongoing star formation in BCGs. Finally, a global red sequence for the XXL-100-GC cluster sample is constructed by applying appropriate k- and distance modulus corrections to transform individual cluster member photometry to a common redshift. The distance of individual BCGs from the global red sequence is then employed to investigate the extent to which the SFH of individual BCGs differs from the average properties of the cluster sample.

4.1 BCG offset from X-ray centroid

As the most massive galaxy within a cluster, the BCG migrates to the centre of the host cluster as a result of dynamical friction. As the
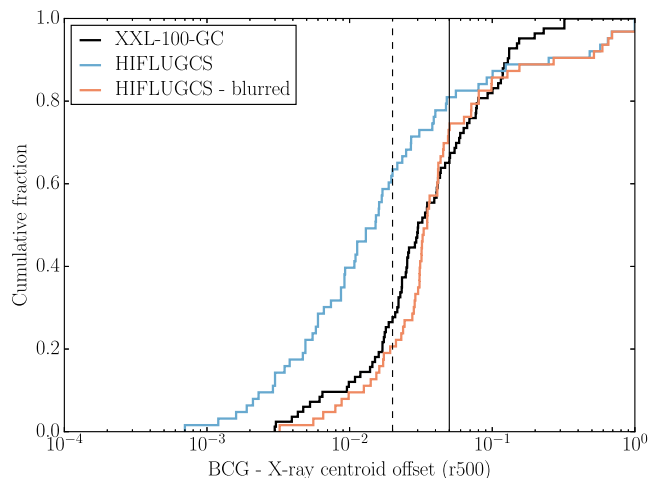
Figure 2. Comparison of BCG offsets from the X-ray centroid for XXL-100-GC (black), HIFLUGCS (blue). The red line represents the HIFLUGCS offset distribution transposed to the median redshift of the XXL-100-GC sample ($z = 0.33$) and modified by a Rayleigh distribution with a scale parameter of 5 arcsec applied to the X-ray centroid position. The dashed and solidvertical lines represent BCG offsets of $0.02 \times r_{500}$ and $0.05 \times r_{500}$, respectively.

X-ray emitting gas provides an effective observational tracer of the cluster potential, the offset between the X-ray centroid and a BCG can be used as an indicator of the relaxation state of a cluster. In a relaxed cluster the offset between the BCG position and the X-ray centroid should approach zero.

We combine X-ray centroid positions and r_{500} values from XXL Paper II with our BCG positions, to compute the centroid offset for the XXL-100-GC BCG sample in units of r_{500} (listed in Table A1). Scaling the offsets by r_{500} offers a suitable normalization method based on the mass distribution in each cluster. The extent of the *XMM* PSF results in an error of approximately 3.6″ (1σ) respectively in RA and DEC in the measured X-ray centroid of moderately bright (>300 counts), extended sources (Faccioli et al., in preparation). Fig. 2 illustrates the effect of this positional error in a comparison of the distribution of BCG offsets in the XXL-100-GC and HIFLUGCS (Zhang et al. 2011) surveys. Although it appears that the XXL-100-GC sample is lacking in low-offset BCGs compared to HIFLUGCS, we demonstrate that this difference is largely a result of the centroid uncertainty of XXL-100-GC clusters. Fig. 2 displays the HIFLUGCS offset distribution transposed to the median redshift ($z = 0.33$) of the XXL-100-GC sample and modified by a Rayleigh distribution with a scale parameter of 5 arcsec (the quadratic combination of the error in both axis) applied to the X-ray centroid (red line). One can see that the effect of this is to scatter low-offset BCGs to higher offsets, bringing the distribution into closer agreement with the XXL-100-GC distribution.

Despite this position error, BCG offsets may still be employed to classify clusters as relaxed or unrelaxed. We select a threshold of $0.05 \times r_{500}$ as it is large enough to be unaffected by the X-ray centroid error over the full range of XXL-100-GC redshifts yet provides physically sensible results when applied in later analyses in this paper. In particular, the angular scale defined by $0.05 \times r_{500}$ for an example cluster at $z = 1$ with $r_{500} = 700$ kpc is two times larger than the angular error in the X-ray centroid. Clusters with a normalized BCG offset from the X-ray centroid lower than $0.05 r_{500}$ will be considered *relaxed*, while those with a larger offset will be considered *unrelaxed*. We note that we have experimented

with varying this threshold, in particular setting the threshold for an unrelaxed cluster as $>0.1 \times r_{500}$. This selection did not change the qualitative nature of the results presented in this paper and resulted in a much smaller sample of clusters classified as unrelaxed (16 instead of 30). Physically, the important distinction therefore appears to be to separate clusters into low-offset, relaxed clusters and the rest.

4.2 X-ray gas concentration

Clusters that display very peaked central X-ray surface brightness profiles may be classified as *cool-core* clusters. Such cool cores in massive clusters are associated observationally with central concentrations of cool X-ray gas and optical emission line filaments which appear to be accreting on to the BCG (e.g. Crawford et al. 1999). Cool-core clusters can be disrupted by cluster scale merging events as a result of the input of kinetic energy from the merger into the cluster ICM (e.g. Ricker & Sarazin 2001). Energy input to the central gas concentration raises it to a higher energy state within the cluster potential, i.e. moves it to larger clustercentric radius. In addition to cluster merging, an AGN outburst in the BCG could also disrupt the properties of a cool-core (e.g. Guo & Oh 2009). Although observed X-ray surface brightness profiles of clusters display considerable variation, they remain an effective indicator of the presence of cool-core within a cluster.

For clusters observed at sufficiently high resolution, the central slope of the X-ray surface brightness profile can be used to estimate the gas concentration and the relaxation state. XXL-100-GC spatial resolution is limited by the relatively large PSF of *XMM–Newton*, making the measurement of the inner slope impractical for the whole sample. Instead we obtain the X-ray gas concentration measurements for XXL-100-GC from Démoclès et al. (in preparation) who compute the c_{SB} parameter defined by Santos et al. (2008) as the ratio of the average surface brightness within 40 and 400 kpc. Santos et al. (2010) and Hudson et al. (2010) show that c_{SB} has a low scatter with cluster central cooling time, making it a reliable indicator of cluster relaxation.

We test the robustness of the method used to measure the c_{SB} parameter in XXL-100-GC by applying the same procedure to mock X-ray images created from the cosmoOWLS simulation (Le Brun et al. 2014). CosmoOWLS is a large suite of smoothed particle hydrodynamics simulations within a cosmological volume that include the effects of a variety of gas physics, such as gas cooling and feedback from supernovae and AGNs. Simulated X-ray images of 25 clusters spanning the whole range of c_{SB} with similar redshift and temperature distributions to XXL-100-GC were created. The simulated images were then folded through the *XMM–Newton* response and convolved with the PSF of the telescope. A realistic background was added to the images to create a mock *XMM–Newton* image similar to real XXL observations. Finally, the same method was applied to measure the concentration parameter of both the mock images and the original simulated data. The median value of $c_{SB, \, mock} - c_{SB, \, true}$ is -0.02 with a scatter of 0.13. Therefore, our method is able to recover the concentration of XXL clusters in a relatively unbiased manner albeit with limited precision. As a final check, in Fig. 3 we compare the distribution of c_{SB} values measured for the XXL-100-GC sample to the HIFLUGCS sample (Hudson et al. 2010). Both samples are area-complete and flux-limited, yet with different mean redshifts, and display c_{SB} distributions that are qualitatively very similar. To highlight how different selection methods affect the resulting sample, an estimate (without PSF correction) of the c_{SB} values for the luminosity-selected LoCuSS sample is also shown (Démoclès, Smith & Martino, private communication).
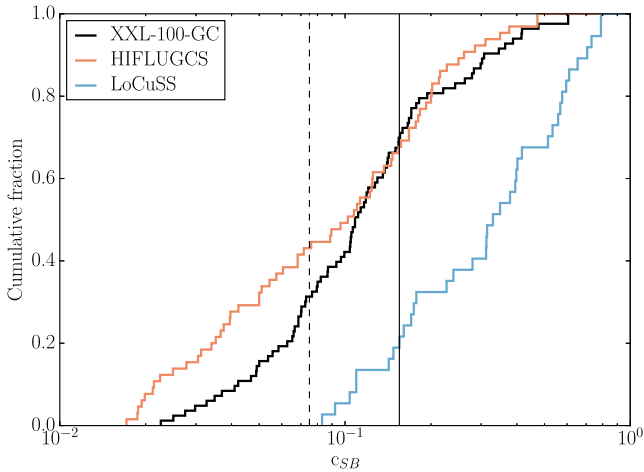
Figure 3. Cumulative fraction of X-ray gas concentration parameter for the XXL-100-GC and HIFLUGCS samples. The dashed and solid vertical lines indicate $c_{SB} = 0.075$ and 0.155, respectively separating each distribution into non-, weak- and strong-cool-core clusters according to Santos et al. (2008).

4.3 BCG stellar masses

Estimating the stellar mass of a BCG requires knowledge of its SFH. Following Lidman et al. (2012), we deduce an average SFH for the BCG sample. We then employ this global SFH to estimate the stellar masses of individual BCGs. As the MegaCam photometry in the W1 field is the most reliable, we derive the SFH of the sample using only these BCGs. This SFH model is then applied to the whole sample assuming that the BCGs in the BCS and DECam fields are physically identical on average to the ones in W1. Extinction in the W1 field is low ($\sim$0.03 z-mag and $\sim$0.01 i–z colour) and is ignored as model uncertainties dominate. W1 photometry has a typical night to night scatter of 0.03 mag that is combined quadratically with each BCGs photometric uncertainty.

We determine the best-fitting SFH model for the XXL-100-GC sample by comparing model stellar populations of varying properties to the sample of BCG colours versus redshift. We employ the *EzGal*[8] PYTHON package to produce the stellar population models and determine the model that best reproduces the observed i–z colours of the W1 BCGs sub-sample. This is achieved by identifying the lowest weighted χ^2 value for a set of models with metallicity Z=0.5, 0.75, 1, 1.5 and 2.5 $Z_\odot$. For each metallicity value, the best-fitting model is sought by varying the time-scale τ of an e-folding model star formation rate between 0 and 10 Gyr and the formation redshift (z_f) between 1 and 5. The process is performed for both a Charlot–Bruzual (CB07) model (Bruzual & Charlot 2003; Charlot & Bruzual, in preparation) with a Salpeter initial mass function (IMF; Salpeter 1955) and a Chabrier IMF (Chabrier 2003). A family of Conroy (C09) models (Conroy, Gunn & White 2009) with Z=$Z_\odot$ and a Salpeter IMF is also used to see if the choice of model greatly influences our final SFH.

Fig. 4 displays the confidence intervals obtained for each set of models. The various models differ little in the parameter space enclosed by their 3σ confidence interval and minimal χ^2 values. We select a CB07 model described by a Salpeter IMF with Z=$Z_\odot$, single stellar population (SSP) and z_f=2.5 as our average SFH because it has the lowest formal χ^2 and this metallicity has a slightly
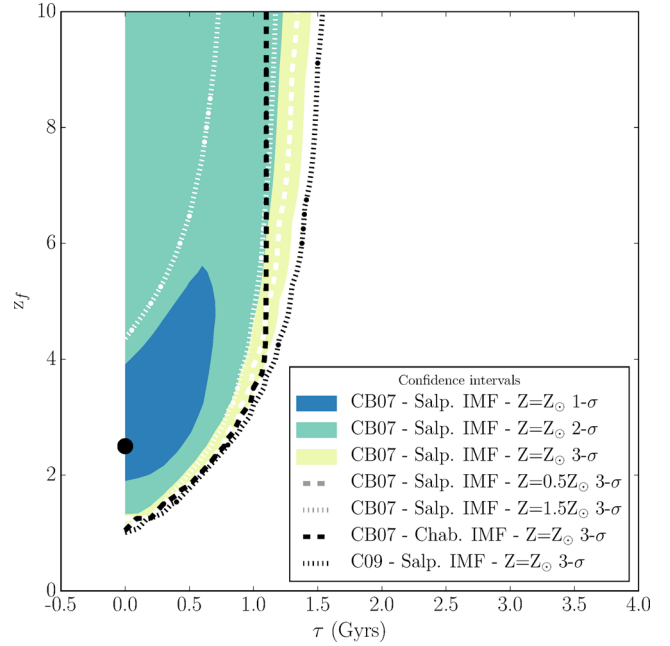
Figure 4. Star formation history confidence intervals contours. The 1σ, 2σ and 3σ contours (respectively shown in blue, green and yellow) representing the quality of the fit between observed BCGs i–z colour evolution and a CB07 model with Z=$Z_\odot$ and Salpeter IMF. The other dashed lines represent various 3σ contours obtained for different IMF or metallicity choices. The fit with the lowest χ^2 value is represented by the black dot and corresponds to CB07 model with a single-stellar population, solar metallicity and Salpeter IMF.

more precisely defined 1σ confidence interval. We prefer the use of a Salpeter IMF as Smith, Lucey & Conroy (2015) demonstrate that a 'bottom-heavy' IMF potentially provides a better description of the SFH of massive galaxies than a 'bottom-light' Chabrier IMF. Our findings are slightly different than those reported by Lidman et al. (2012) yet overall agree at the 2σ confidence level. Furthermore Lidman et al. (2012) also employ J–K colours to constrain the average SFH, which is less sensitive to recent star formation than our i–z colours.

Fig. 5 indicates how metallicity, SFH and the redshift of formation affect the predicted values of colour and z-band magnitude. Maintaining the same SFH, one notes that though metallicity variations act to offset the predicted colours they do not significantly alter the z-band magnitude, our proxy for stellar mass. The SFH with a non-zero τ generates bluer galaxy colours at high redshift. Even a small positive value of τ is in tension with the colours observed for high-z BCGs in XXL-100-GC, pointing towards passive evolution since early times. We note that none of the models works completely, some BCGs being bluer in i–z than any of our model can reproduce.

Employing the best-fitting model within our adopted cosmology, we apply a simple bisection algorithm to obtain the absolute z-band magnitude that best reproduces the observed magnitude of each BCG. DECam z-band magnitudes are used for BCGs in the XXL-S field. Stellar masses are obtained by applying a mass-to-light ratio appropriate for the SFH model to each BCG z-band luminosity. The effect of switching between an assumed Chabrier or Kroupa IMF is to change the derived stellar masses equally over the XXL-100-GC sample without introducing any IMF-dependent evolution with redshift. The influence on the relations derived from BCG masses is also marginal. The uncertainties in Table A1 represent the range
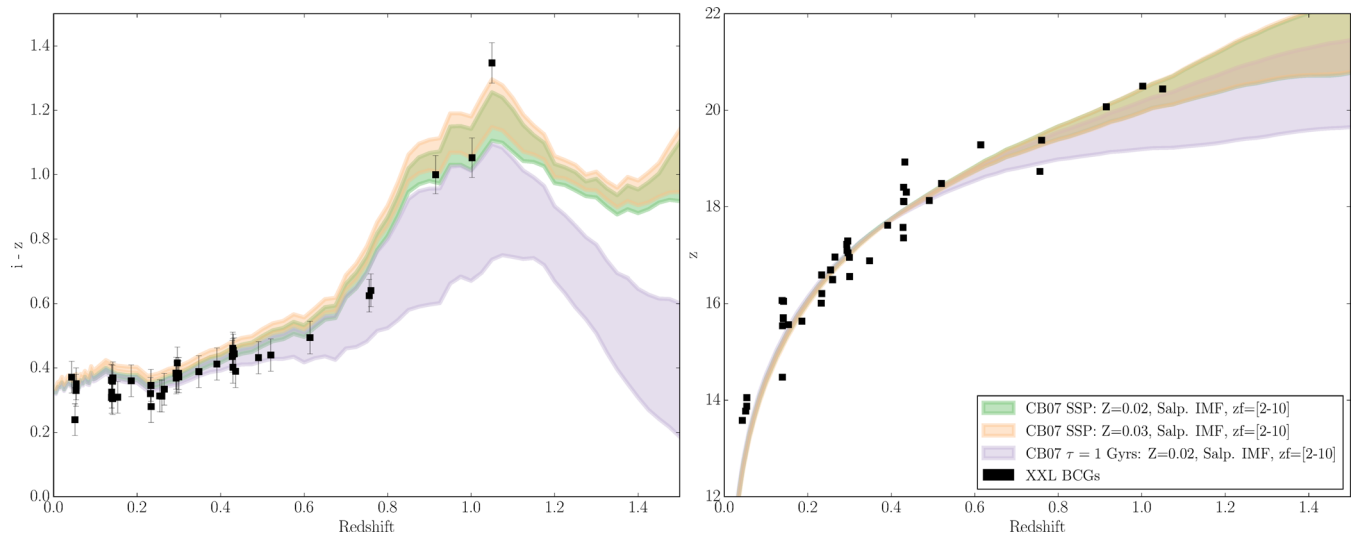
Figure 5. Colour (left) and z-band magnitude (right) evolution of the XXL-100-GC North subsample. The green band represents the evolution of the best-fitting model for z_f between 2 and 10 with solar metallicity and Salpeter IMF. The red band is the same model with $1.5 \times Z_\odot$ and the blue band is a model with solar metallicity and $\tau = 1$ Gyr. The black squares represent XXL-100-GC North BCGs. Both panels use the same legend.

of masses within the 1σ confidence interval shown in Fig. 4. As one can see from the shaded regions in Fig. 5, model errors become more important at higher redshift. Because of this, model errors dominate mass uncertainties for all BCGs. Resulting mass uncertainties are $\sim 10 - 20$ per cent, somewhat higher than the $\sim 5 - 10$ per cent obtained with a similar method by Lidman et al. (2012) without model errors. Additionally, masses obtained from a reprocessing by the Portsmouth Group of SDSS DR12[9] following Maraston et al. (2013) are available for 30 BCGs. Values determined for our BCGs fall within ± 0.2 dex of the masses they report for a passive model with Salpeter IMF.

4.4 M_{cluster}–M_{BCG} relation

It is generally accepted that more massive BCGs exist in more massive clusters. In the hierarchical scenario, as massive clusters grow by the accretion of less massive sub-units, recently accreted galaxies migrate to the centre of the cluster potential where they are themselves accreted by the BCG which itself grows in mass. The relationship between cluster and BCG mass may be expressed as a simple power-law relationship of the form $M_{\mathrm{cluster}} = A \times M_{\mathrm{BCG}}^n$. Various measurements of the power-law exponent n for can be found in the literature for cluster samples typically limited in mass to $M_{\mathrm{cluster}} > 10^{14}$ M$_\odot$. Stott et al. (2010) find a power-law index of 2.4 $\pm$ 0.6 for a sample of 20 $z > 0.8$ X-ray luminous clusters identified from either their X-ray emission or various optical methods. Stott et al. (2012) obtain an index of 1.3 ± 0.1 from 103 clusters chosen from the XCS first release by applying a redshift cutoff of $z < 0.3$. Finally, Lidman et al. (2012) combine data from Stott et al. (2010) and Stott et al. (2012) with a sample of SpARCS clusters identified as galaxy overdensities in deep IR observations to obtain an index of 1.6 ± 0.2.

XXL-100-GC provides an important perspective on the relationship between BCG and cluster masses as it samples a range of clusters masses typically lower than those studied in the literature and because it includes additional diagnostic information on the

Table 2. Properties of the $M_{\mathrm{cluster}} = A \times M_{\mathrm{BCG}}^n$ fits shown in Fig. 6.

Case	n	log$A$	#
All clusters	0.84 ± 0.09	4.33	85
c_{SB} weighted	1.04 ± 0.24	1.79	–
$(c_{\mathrm{SB}})^{-1}$ weighted	0.55 ± 0.16	7.89	–
BCG offset $<0.05 \times r_{500}$	1.03 ± 0.10	1.97	55
BCG offset $>0.05 \times r_{500}$	0.46 ± 0.17	8.88	30

relaxation state of each cluster. For the purpose of this analysis we assume that a relaxed cluster is either characterized by the presence of a cool-core, indicated by a high value of c_{SB}, or a dynamically relaxed BCG, indicated by a low value of normalized offset from the centroid.

We therefore perform a number of fits to the slope of M_{BCG} versus M_{cluster} employing different assumptions. The best fit was obtained employing χ^2 minimization and resampling the data 100 000 times assuming data uncertainties are normally distributed, taking the median index value and standard deviation. The results are indicated in Table 2 and in Fig. 6. We perform an unweighted fit to the mass data points to provide a baseline description of the relationship. We also perform a fit employing cluster c_{SB} values as a simple weighting function in order to weight the contribution of relaxed clusters in the relationship. A similar fit employing inverse c_{SB} values weights the relationship towards unrelaxed clusters. Finally we also perform fits using only clusters with BCGs located at small or large offset radii to perform an alternative description of the relationship for relaxed or unrelaxed clusters, respectively.

The fit results for BCGs located in relaxed clusters is consistent with the scenario where the BCG stellar mass is proportional to the total cluster mass. The fit normalization is such that the BCG stellar mass represents an approximately constant 1 per cent of the total cluster mass. The fit results also indicate that, at fixed cluster mass, BCGs in unrelaxed clusters are less massive than BCGs in relaxed clusters by up to 0.5 dex. This impression is characterized by the trend for BCGs in unrelaxed clusters to lie predominantly to the left of the M_{BCG} versus M_{cluster} relationship defined by relaxed clusters as shown in Fig. 6. To test the significance of this trend, we define
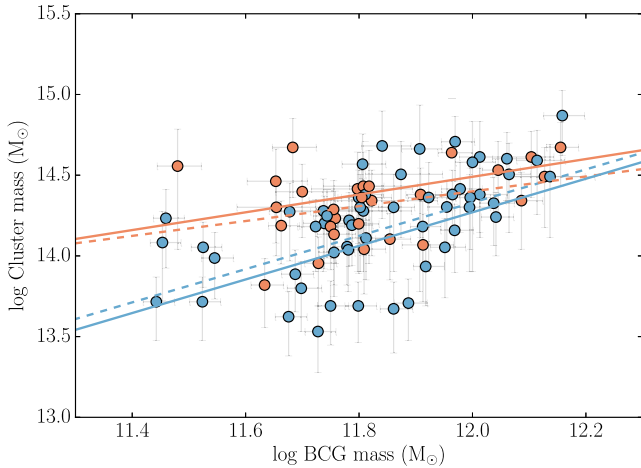
Figure 6. Cluster mass versus BCG mass for XXL-100-GC clusters. Points are colour-coded to emphasize the distribution of clusters exhibiting different relaxation states. The two colours for dots represent BCG offsets of $<0.05 \times r_{500}$ (blue) and $>0.05 \times r_{500}$ (red). The dashed blue and red lines respectively indicate the result of linear fits to clusters of BCG offset $<0.05 \times r_{500}$ and $>0.05 \times r_{500}$. The solid blue and red lines respectively indicate the result of linear fits to clusters of weighted by the value of c_{SB} and inverse c_{SB}.
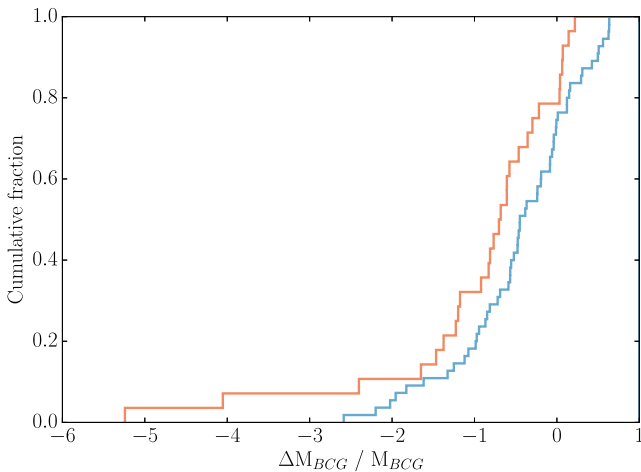

Figure 7. Cumulative normalized BCG ΔM for offsets greater than $0.05 \times r_{500}$ (red) and smaller than $0.05 \times r_{500}$ (blue).

a simple normalized distance measure from the relaxed relation. For each BCG, we measure the distance between the expected BCG mass at the host cluster mass, normalized by the BCG mass (denoted $\Delta M/M_{BCG}$). In other words, the difference between the BCG mass and how massive is the BCG expected to be if it were in a relaxed cluster with its host cluster mass.

Fig. 7 shows the cumulative distribution of BCGs mass lag measurement $\Delta M/M_{BCG}$. A Shapiro test for normality reveals that BCGs located in relaxed clusters are normally distributed (although the mean is not zero) while the BCGs located in unrelaxed clusters are not and follow more closely a lognormal distribution. To compare the distributions, we employ an Anderson–Darling test. This non-parametric test is used to assess whether or not two samples come from the same distribution by computing the maximum deviation between their cumulative distribution. It is very similar to the Kolmogorov–Smirnov (KS) test but differs in that it is better suited to samples with different mean values or outliers. We find that we can reject the null hypothesis that the samples are drawn

from the same distribution with 95 per cent confidence (p-value $<$ 0.05), a value that goes up to 99.6 per cent (p-value $<$ 0.004) if we compare clusters with offset lower than $0.05 \times r_{500}$ to ones with offsets greater than $0.1 \times r_{500}$.

4.5 Δm_{12} and the BCG merger history

The luminosity gap between the first and second brightest cluster members, Δm_{12}, provides a measure of cluster galaxy evolution. The hierarchical accretion model of galaxy growth predicts that the BCG within a cluster should grow in mass faster than noncentral, non-dominant galaxies as the BCG is located at the centre of the cluster potential to which less massive galaxies migrate via dynamical friction. Therefore, if BCGs grow via such accretion, one expects the luminosity gap to grow with every accreted galaxy (e.g. Smith et al. 2010; Raouf et al. 2014). Cluster-scale merger events can affect the evolution of Δm_{12} as they can add bright galaxies, reducing the luminosity gap.

To compute Δm_{12} for each cluster we first define cluster membership. Since have we only photometric redshifts for most non-BCG galaxies, we put stringent constraints on the membership classification to reduce contamination. We define a galaxy as a member of a given cluster if the cluster redshift is within the 1σ range of the photometric redshift of the galaxy and the galaxy lies within $1 \times r_{500}$ of the X-ray centroid. If the galaxy has a spectroscopic redshift, it is used instead of the photometric redshift. A galaxy then has to be within 3000 km s^{-1} of the cluster to be considered a member. We then set the value of Δm_{12} as the difference in z-mag between the BCG and the second brightest member.

We apply a Spearman rank correlation test to determine the extent to which Δm_{12} is correlated with measurements of BCG mass and mass-lag $\Delta M/M_{BCG}$ across the XXL-100-GC sample. Noting that one also expects Δm_{12} to increase with time, we compute correlation values correcting for any partial correlation with redshift according to the formula:

$$S_{AB|C} = \frac{S_{AB} - S_{AC}S_{BC}}{\sqrt{(1 - S_{AC}^2)(1 - S_{BC}^2)}},$$

where $S_{AB|C}$ is the Spearman rank correlation between A and B, corrected for C. This test indicates that Δm_{12} is correlated positively with BCG mass and $\Delta M/M_{BCG}$ at 99.5 per cent and 99.8 per cent confidence level, respectively and that Δm_{12} is a reliable tracer of BCG mass growth. Individual values of Δm_{12} can be found in Table A1.

The value of Δm_{12} does not indicate the mass distribution of accreted galaxies. To address this question we consider the results on BCG growth taken from the Millennium Simulation (Springel et al. 2005) at $z < 1$ using the `DeLucia2006a` semi-analytical galaxy models data presented in De Lucia & Blaizot (2007). These models were obtained from the Millennium database[10] (Lemson 2006). One hundred BCGs were randomly selected at $z = 0$ from clusters with $M_{cluster} \sim 2 \times 10^{14} M_{\odot}$, i.e. the average XXL-100-GC cluster mass. For each BCG we obtain the merger tree between $z = 1$ and $z = 0$ (Lemson & Springel 2006).

Fig. 8 shows the distribution of the number of mergers in bins of mass ratio for the 100 BCGs in addition to the fractional contribution to the $z = 0$ BCG mass. From the figure it is clear that one-half of the $z = 0$ BCG mass is contributed from mergers at mass ratios greater than and less than a value of 1: 3. Although there is a certain
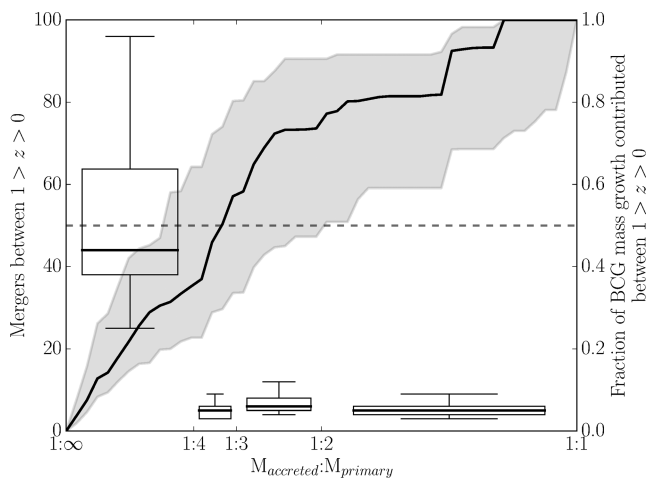
---

[10] http://gavo.mpa-garching.mpg.de/portal/

Figure 8. Accretion history over $0 < z < 1$ obtained for 100 semi-analytical BCG galaxy models realized within `DeLucia2006a`. The rectangular boxes indicate the number of mergers for mass ratio intervals of $1: \infty - 1: 4$, $1: 4 - 1: 3$, $1: 3 - 1: 2$ and $1: 2 - 1: 1$. The top and bottom of each box marks the upper and lower quartile values while the interior horizontal line indicates the median value. The error bars indicate the 5th and 95th percentiles. The solid black line indicates the median value of the normalized cumulative merger contribution to BCG mass growth. The accompanying shaded grey region indicates the full extent of the 100 normalized cumulative mergers to the BCG mass growth. The grey horizontal dashed line indicates the point at which the BCG has accreted 50 per cent of its $z = 0$ mass.

amount of scatter about the mean relationship displayed in Fig. 8, the results from simulations appear to be in broad agreement with those of Burke & Collins (2013) obtained with *HST* imaging of BCGs and their bound companions around $z \sim 1$.

4.6 Luminosity segregation

An alternative diagnostic of the hierarchical accretion of cluster galaxies is to consider their luminosity segregation. A prediction of this hypothesis is that the central regions of a galaxy cluster should be overabundant in bright galaxies relative to faint as brighter (i.e. more massive) galaxies are expected to migrate faster to the cluster centre under the influence of dynamical friction. One further expects that this overabundance of bright galaxies will be more marked in relaxed clusters compared to those which are unrelaxed.

The luminosity segregation method proposed by Lidman et al. (2013) compares the cumulative spatial distribution of bright galaxies to faint ones. They employ a two sample KS test on the two distributions and find a significant difference in the radial distribution of faint and bright galaxies yet note that this result is very sensitive to the arbitrary maximum radius to which the calculation is performed. Unlike Lidman et al., we know the value of r_{500} for all the clusters and use it as the maximum radius. Although still arbitrary, the use of r_{500} as the maximum radius used in the same calculation applied to the XXL-100-GC sample does at least provide a consistent and physically motivated maximum radius for each cluster.

We compare the cumulative radial distribution of bright and faint cluster members in XXL-100-GC clusters. We define bright galaxies as the 2nd, 3rd and 4th brightest members. Faint galaxies are defined as the 10th–40th brightest members. Fig. 9 shows the cumulative distributions of faint and bright galaxies within r_{500} for the relaxed and unrelaxed clusters. A two-sample Anderson–Darling
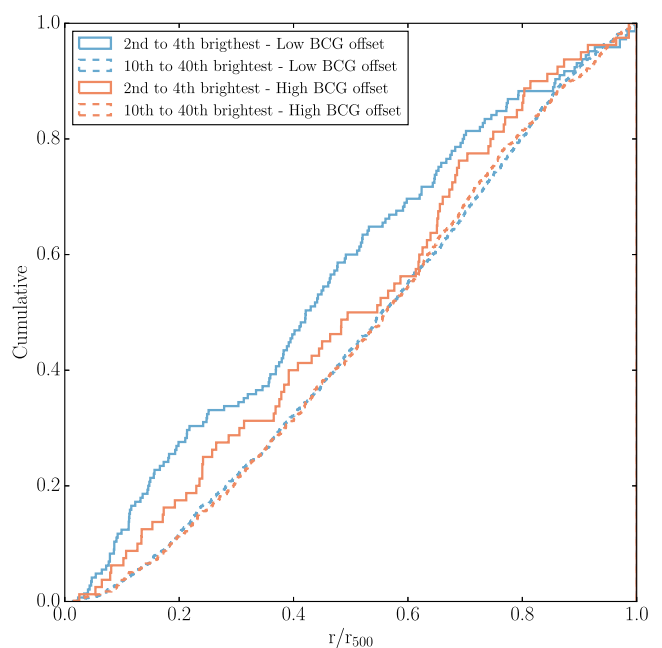

Figure 9. The cumulative radial distribution of bright and faint galaxies in relaxed ($<0.05 \times r_{500}$) and unrelaxed ($>0.05 \times r_{500}$) clusters. The solid blue and red lines shows the distribution of 2nd–4th brightest members in relaxed and unrelaxed clusters. The dashed blue and red lines show the distribution of 10th–40th brightest galaxies in relaxed and unrelaxed clusters.

test reveals that the radial distribution of bright galaxies in unrelaxed clusters (*red*) is not very different than that of faint ones (*p*-value = 0.13, 30 clusters). However, in relaxed clusters (*blue*) a significant difference exists (*p*-value=1.97×10^{-5}, 55 clusters).

4.7 Hα star formation

BCGs typically appear as passively evolving stellar populations. However, observed stellar masses grow by a factor ~ 2 between $z = 1$ and the present epoch (Lidman et al. 2012). Active star formation in BCGs is observed and in the literature has been interpreted as evidence for inflows of cool gas within the cluster potential (e.g. Donahue, Stocke & Giola 1992; Edge, Stewart & Fabian 1992; O'Dea et al. 2010). Evidence of active star formation associated with an infall of gas from cooling flows is also observed by Sanderson, Edge & Smith (2009) in the spectra of some BCGs in the LoCuSS sample. We assess the presence of active star formation in the sample of XXL-100-GC BCGs by focusing on a sub-sample of 30 BCGs in the Northern field with $z \lesssim 0.5$ for which Hα emission fluxes have been measured by the SDSS Portsmouth group from dust extinction-corrected DR12 data (Thomas et al. 2013).

Although the spectra have high signal-to-noise ratio (SNR), only half of the BCGs show Hα emission detection with a line SNR $\gtrsim$ 2 down to an observed flux of $\sim 1 \times 10^{-17}$ erg cm^{-2} s^{-1}. Using the classical Hα flux to SFR conversion from Osterbrock & Ferland (2005) and the stellar masses we determined in Section 4.3, we confirm that none of the $z \lesssim 0.5$ BCGs in XXL-N shows a sSFR greater than $\sim 10^{-12}$ yr^{-1}. While the exact value of the star formation rate expected for a passive BCG is unclear, observations and simulations provide some guidance. Zwart et al. (2014) use 1.4GHz VLA data from a K_S selected sample of galaxies in the VIDEO survey to deduce a sSFR of $\sim 10^{-11}$ yr^{-1} for $\sim 10^{11}$ [$M_\star/M_\odot$] elliptical
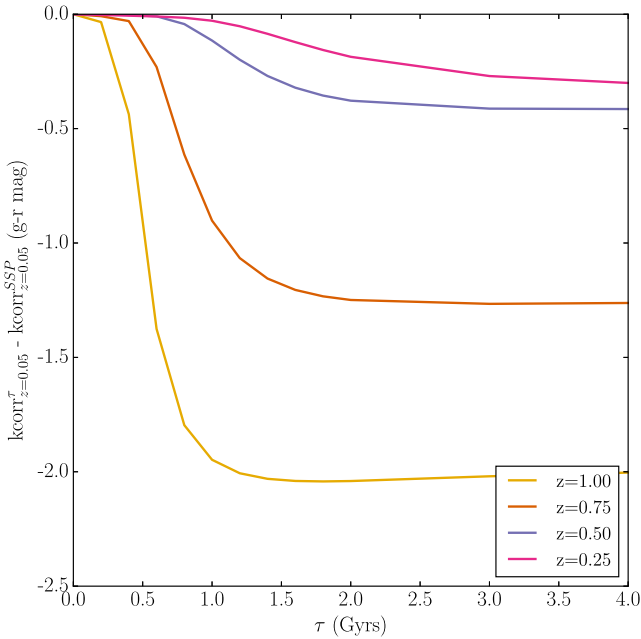
Figure 10. The difference in *k*-correction required to correct a galaxy at a specified observed redshift to $z = 0.05$ assuming a SSP and an exponentially decreasing star formation rate of time-scale τ.

Figure 11. The colour–magnitude diagram of all XXL-100-GC North (top panel) and South (bottom panel) member galaxies *k*-corrected to $z = 0.05$ considering an SSP star formation history. The grey dotted lines show the initial red-sequence lower colour limit obtained from the double Gaussian fit. The solid black lines show the converged red-sequence colour cutoff. The red dots indicate all red-sequence galaxies with $M_V \leq -20$; The blue squares indicate BCGs. The black dashed lines show the best-fitting red-sequence relation.

galaxies with $0 < z < 1$. Henriques et al. (2012) find a sSFR of $\sim 10^{-12}$ yr^{-1} for similar masses and redshift in simulations.

We therefore conclude that none (less than 3 per cent) of $z < 0.5$ XXL-100-GC BCGs display evidence for enhanced star formation above that expected for field ellipticals of comparable mass and redshift. It is important to note that we do not possess any spectroscopic emission line constraint on the current SFR in $z > 0.5$ XXL-100-GC BCGs.

4.8 Red-sequence offset

The analysis of XXL-100-GC BCG stellar masses (Section 4.3) and Hα emission line fluxes at $z \lesssim 0.5$ (Section 4.7) indicate that these BCGs display low specific star formation rates. However, we note that because of a combination of the wavelength coverage of SDSS spectroscopy and the fact that the majority of BCGs are located at $z < 0.5$, these tests are weighted towards the properties of low-redshift BCGs within the XXL-100-GC sample. There are 19 BCGs at $z > 0.5$, meaning we are left uninformed on possible star formation in a fifth of the sample. This section tries to address this with an alternative test of star formation in XXL-100-GC BCGs based on the magnitude of BCG colour offsets from their host cluster red sequences. As Fig. 10 indicates, the *k*-correction applied to galaxies at greater redshift is more sensitive to deviations from the assumption that BCG spectra are described by an old, passively evolving SSP.

We separately create a single stacked colour–magnitude diagram for all cluster member galaxies located within each of the XXL-N and XXL-S fields. We apply a *k*-correction based upon the best-fitting SFH obtained in Section 4.3 and a distance modulus correction to stack all member galaxy photometry at an assumed $z = 0.05$. Member galaxies are selected employing the criteria outlined in Section 4.5. We determine the location of the stacked cluster red sequence on each colour–magnitude diagram employing an iterative process. First, considering only galaxies with $M_V \leq -20$,
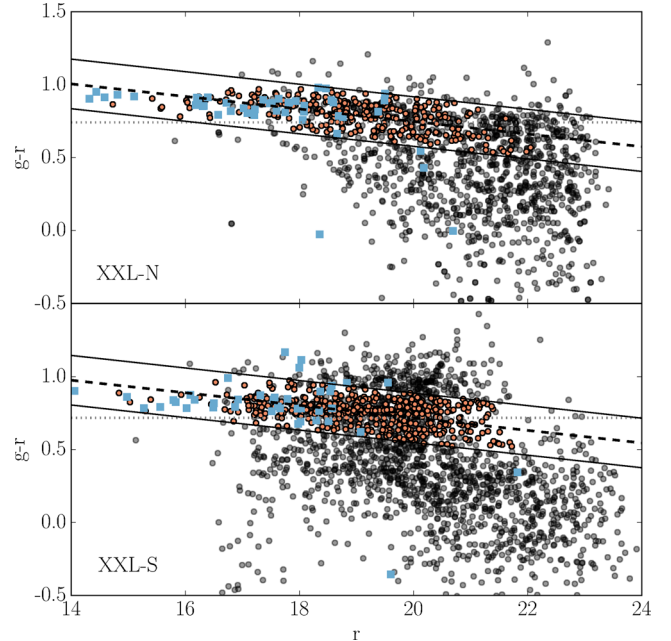
we fit a simple double Gaussian distribution to the colour distribution of member galaxies and define the red-sequence cutoff as the colour at which the contribution of blue and red galaxies are equal. We then fit a linear red sequence from those galaxies redder than this cutoff and, using the $\Delta(B - V) = -0.2$ criterion for blue galaxies from Butcher & Oemler (1984), we refine the red sequence by re-selecting red galaxies as the ones for which $g - r$ colour falls within $\Delta(B - V) = \pm 0.2$ of the linear fit. This process is repeated until it converges and the slope in XXL-S is fixed to be the same as the one in XXL-N. Doing so makes the red sequence in XXL-S slightly steeper but limits the contribution of the large number of dubious $g - r > 1.0$ galaxies in the field that may be caused by the larger photometric errors in this field. Fig. 11 shows the resulting colour–magnitude diagram (corrected to SDSS $g - r$) of all member galaxies from both fields after *k*- and distance modulus correction.

The resulting distribution of BCG offsets from the stacked red sequence in each field is consistent with a Gaussian distribution of zero mean. In both XXL-N and XXL-S, the distribution has a standard deviation $\sigma(g - r) \approx 0.07$: a relatively small deviation that indicates that most BCGs lie close to the red sequence. It is perhaps no surprise that the XXL-100-GC BCGs lie at low colour offset from the red sequence: these represent the bulk of the systems for which we have good quality spectroscopy and to which the SFH analysis applied in Section 4.3 is most sensitive.

As mentioned previously, earlier analyses indicate that XXL-100-GC BCGs have passively evolving SFHs. However, Fig. 10 indicates that the *k*-correction applied to transform a BCG at $z > 0.5$ to the $z = 0.05$ colour–magnitude plane is very sensitive to deviations from an assumed old, co-eval SSP model. SSP models computed assuming $\tau \leq 1$ Gyr fall within our $3 - \sigma$ confidence limits displayed in Fig. 4. One can therefore employ the absence of

BCGs with $z > 0.5$ and large colour offsets from the stacked red sequence as evidence that these systems are also consistent with SSP models possessing $\tau \leq 1$ Gyr. In fact, out of the 19 BCGs at $z > 0.5$, we find only one with an offset that can only be explained with a $\tau \gtrsim 1$ Gyrs: XLSSC 546. It is unfortunate that this system lacks a spectroscopic redshift which might indicate the presence of active star formation. However, a closer inspection of the X-ray contours of XLSSC 546 reveals that the BCG sits within one of two X-ray peaks observed in the cluster, suggesting the cluster is disturbed and possibly experiencing a merger event.

5 DISCUSSION

We have determined that, within the sub-sample of relaxed XXL-100-GC clusters, the BCG stellar mass is linearly related to the cluster weak-lensing mass. We compute a value of $n = 1.04 \pm 0.20$ and 1.03 ± 0.10, respectively for the power-law index of the $M_{cluster}$–M_{BCG} relation for XXL-100-GC clusters which appear relaxed either via their c_{SB} weighting or based upon low BCG offset ($<0.05 \times r_{500}$). These index values are generally lower than reported in the literature and may be due to three considerations: (1) the XXL-100-GC sample extends to lower mass clusters, (2) we explicitly differentiate between relaxed and unrelaxed systems and (3) flux-selected samples like XXL-100-GC and HIFLUGCS contain a larger fraction of disturbed systems compared to luminosity selected cluster samples. Lower cluster mass correlates with lower member galaxy velocity dispersions (Willis et al. 2005). As the cluster velocity dispersion approaches that of the BCG, the effective merger cross-section increases rapidly (e.g. Makino & Hut 1997). This assertion is supported by various analysis (e.g. Gonzales, Zaritsky & Zabuldoff 2007; Leauthaud et al. 2012; Coupon et al. 2015; Ziparo et al. 2016) that indicate that BCGs contribute a greater fraction of the total cluster stellar luminosity in lower mass clusters, as expected if stellar mass is more efficiently accreted by the BCG.

Perhaps more important than the exact value of the slope of the $M_{cluster}$–M_{BCG} relation is the result that relation is statistically different for relaxed and unrelaxed clusters. The relation for clusters with a disturbed BCG is much shallower at $n = 0.55 \pm 0.16$ and 0.46 ± 0.17, respectively for clusters weighted by inverse c_{SB} or for large BCG offset ($>0.05 \times r_{500}$). This indicates that, when a cluster gains mass via a merger, the BCG stellar mass initially lags behind the value expected for a dominant galaxy in a cluster with the mass of the merged host. The effect of a cluster-scale merger is therefore more readily detectable via the increased cluster mass (inferred from the ICM temperature) rather than the stellar mass of the BCG.

Although star formation in BCGs can be caused by the infall of gas from cooling flows, XXL-100-GC clusters display low central gas concentrations. Within XXL-100-GC we have used spectroscopic observations of the Hα line as a direct star formation indicator for a third of the sample. We find no Hα-determined sSFRs above the value observed in similar mass, passive galaxies in the field.

Furthermore, the analysis of BCG offsets from the global cluster red sequence indicates that only one high redshift BCG in XXL-100-GC, located in a potentially merging cluster, shows evidence for a stellar population described by a declining star formation rate of time-scale $\tau \gtrsim 1$ Gyr. In fact, the almost complete absence of active star formation observed in the BCG population motivates our choice of an SSP model to describe the SFH of XXL-100-GC BCGs. The population of XXL-100-GC BCGs therefore appears

to be homogeneously passive irrespective of the relaxation state of the parent cluster. This realization is in agreement with results from Webb et al. (2015) and McDonald et al. (2016) indicating that dry mergers are the dominant source of growth in BCGs at $z \lesssim 1$. Another important factor at play is that XXL-100-GC clusters are less massive on average than their LoCuSS and CLASH counterparts. Liu, Mao & Meng (2012) show that the incidence of star formation in BCGs increases with cluster richness and X-ray luminosities, both cluster mass proxies. In agreement with what we report in this work, XXL-100-GC clusters should host BCGs with significantly lower star formation on average than those in the LoCuSS and CLASH sample.

Fig. 9 indicates that bright galaxies have a dominant contribution at low radii in clusters with a BCG offset of $<0.05 \times r_{500}$. In this case, an Anderson–Darling test between bright and faint galaxies indicates that we can exclude that they come from the same distribution at >99.99 per cent. The same test applied clusters with a BCG offset of $>0.05 \times r_{500}$ cannot exclude the null hypothesis. The test suggests that, as the cluster evolves, so does the galaxy distribution. This is important as such infalling bright galaxies could present a major source of BCG stellar mass growth via major mergers as they contribute typically half of the BCG growth according to Burke & Collins (2013) and our results from Section 4.5. However, we note that the statistical significance varies according to what we define as a *bright* or *faint* galaxy. Nevertheless, the results generally indicate the presence of mass segregation.

In Fig. 12, we attempt to combine a number of observational measures to generate an overview of BCG evolution in galaxy clusters. The leftmost panel of Fig. 12 reveals that we observe no XXL-100-GC BCGs with a high-mass lag (negative values) in clusters where the X-ray gas is very relaxed. The BCG is clearly gaining stellar mass and reducing the inferred mass lag before the bulk of the X-ray gas can settle in the cluster potential. This point is relevant as the XXL-100-GC BCGs show essentially no evidence for active star formation. This in turn indicates an absence of significant gas accretion as the gas remains disturbed on time-scales longer than stellar mass accretion to the BCG.

The middle panel of Fig. 12 shows that the BCG grows in stellar mass relative to the total cluster mass as the BCG moves towards the centre of the X-ray emitting gas (which we interpret as the centre of the cluster potential). A range of trajectories appear to converge towards the upper-left corner of the diagram (zero mass lag), indicating a certain amount of scatter in the stellar mass growth history of individual BCGs. However, despite this scatter, the absence of points in the lower-left region of the diagram indicates that there exist no relaxed clusters in which the BCG displays a significant mass lag.

The right-hand panel in Fig. 12 indicates that the stellar mass in the BCG grows relative to the second BCG (a similar trend is observed whether one employs the 2nd, 3rd or 4th brightest galaxy as a reference) as it also grows relative to the total cluster mass. The analysis of luminosity segregation contained in Section 4.6 indicates that bright galaxies in relaxed clusters are preferentially located at low cluster centric radius compared to both bright galaxies in unrelaxed clusters and faint galaxies in all clusters. We interpret this result as the effect of dynamical friction operating undisturbed in relaxed clusters. The accretion of such bright, infalling galaxies on to XXL-100-GC BCGs provides a compelling statistical explanation for the trend of Δm_{12} versus mass lag shown in the right-hand panel of Fig. 12 and appears to agree well with simulations which indicate that major mergers might contribute 50 per cent on average of the stellar mass growth in BCGs at $z < 1$.
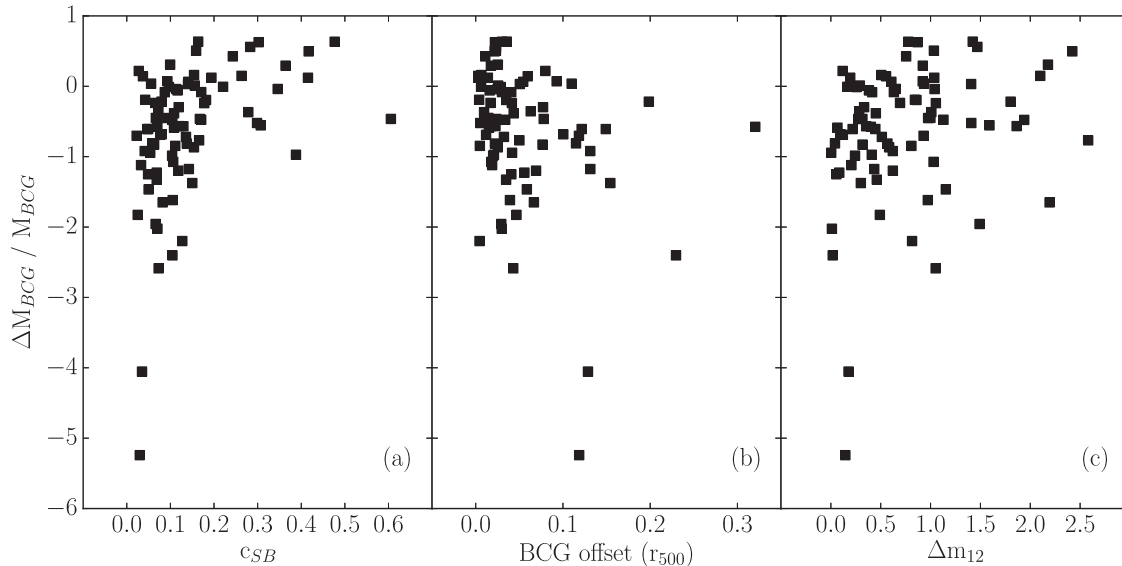
Figure 12. Normalized ΔM_{BCG} for various indicators. The value of ΔM_{BCG} is the difference between a BCG observed mass and the *expected* mass for a BCG in a relaxed cluster of the same mass obtained from the M_{cluster}–M_{BCG} relation. (a) Cluster relaxation from c_{SB}. (b) Dynamical relaxation from BCG offset. (c) Δm_{12} tracing BCG accretion.
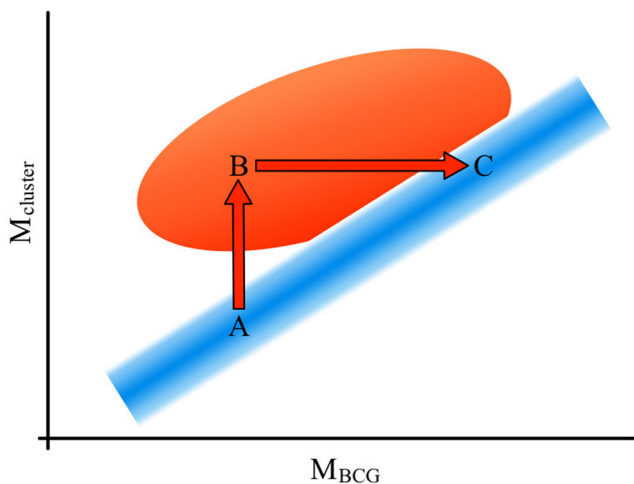

Figure 13. Cartoon of the BCG mass growth through dry merger in XXL-100-GC. The *blue* region represents the expected relation for relaxed clusters while the *red* region is where disturbed clusters are found due to their BCG mass lag.

Finally, BCGs at low-, intermediate- and high-z all broadly cover the same regions of Fig. 12. This impression can be further verified by the application of a Spearman rank correlation test. For all indicators (c_{SB}, BCG offset and Δm_{12}), we find no significant difference in the correlation with BCG mass lag when performing a regular test compared to a partial test correcting for redshift. This would appear to indicate that, although the merger rate of clusters may vary in a secular fashion with cluster mass and redshift, the physical response of the BCG to these stochastic events is independent of redshift.

CONCLUSION

The story told by XXL-100-GC can be summarized by a cartoon presented in Fig. 13. In this scenario, an idealized cluster is initially relaxed and the BCG mass is such that it lies at point A, in agreement with the relationship $M_{\text{BCG}} \propto M_{\text{cluster}}$. Following a cluster-scale merger event, the cluster mass increases and the ICM of the merged cluster is shock heated to the virial temperature of the new system. Any cool-core system present is disrupted and the BCG is displaced from the centre of the cluster potential. At this moment, the system is located at point B in Fig. 13: the ICM temperature reflects the total mass of the system but the BCG now lags in mass relative to the cluster. As the cluster begins to relax, the BCG and other bright galaxies preferentially migrate to the cluster centre under the influence of dynamical friction. These bright galaxies ultimately merge with the BCG, both increasing the BCG stellar mass relative to the cluster and increasing the value of Δm_{12}. At this instance in time the cluster approaches point C on Fig. 13.

Despite the outline above several questions remain: Can the rate of BCG stellar mass accretion be quantified by searching for morphological evidence of merging in high-spatial resolution images of BCGs (e.g. Liu et al. 2015)? In addition, how does the relationship between M_{cluster} and M_{BCG}, which is observed to steepen in cluster samples of greater mass (Stott et al. 2010; Lidman et al. 2012; Stott et al. 2012), depend upon the inferred relaxation state? At what cluster mass does cooling-flow induced BCG star formation become an important mechanism for BCG stellar mass growth (e.g. Sanderson et al. 2009)? A sensible extension to this work would therefore be to study the properties of BCG mass lags in a sample of clusters of higher typical mass than XXL-100-GC.

Hawaii. This work is also based in part on data products produced at Terapix available at the Canadian Astronomy Data Centre as part of the Canada-France-Hawaii Telescope Legacy Survey, a collaborative project of NRC and CNRS.

This research uses data from the VIMOS VLT Deep Survey, obtained from the VVDS data base operated by Cesam, Laboratoire d'Astrophysique de Marseille, France.

Based in part on data acquired through the Australian Astronomical Observatory

This paper uses data from the VIMOS Public Extragalactic Redshift Survey (VIPERS). VIPERS has been performed using the ESO Very Large Telescope, under the 'Large Programme' 182.A-0886. The participating institutions and funding agencies are listed at http://vipers.inaf.it.

GAMA is a joint European-Australasian project based around a spectroscopic campaign using the Anglo-Australian Telescope. The GAMA input catalogue is based on data taken from the Sloan Digital Sky Survey and the UKIRT Infrared Deep Sky Survey. Complementary imaging of the GAMA regions is being obtained by a number of independent survey programmes including GALEX MIS, VST KiDS, VISTA VIKING, WISE, Herschel-ATLAS, GMRT and ASKAP providing UV to radio coverage. GAMA is funded by the STFC (UK), the ARC (Australia), the AAO, and the participating institutions. The GAMA website is http://www.gama-survey.org/.

Funding for SDSS-III has been provided by the Alfred P. Sloan Foundation, the Participating Institutions, the National Science Foundation, and the US Department of Energy Office of Science. The SDSS-III web site is http://www.sdss3.org/.

Based in part on data acquired through the Australian Astronomical Observatory, under programmes A/2013A/018 and A/2013B/001,and on observations at Cerro Tololo Inter-American Observatory, National Optical Astronomy Observatory (NOAO Prop. IDs 2013A-0618 and 2015A-0618), which is operated by the Association of Universities for Research in Astronomy (AURA) under a cooperative agreement with the National Science Foundation. This project used data obtained with the Dark Energy Camera (DECam), which was constructed by the Dark Energy Survey (DES) collaboration.

This paper uses data from observations made with the William Herschel Telescope operated on the island of La Palma by the Isaac Newton Group in the Spanish Observatorio del Roque de los Muchachos of the Instituto de Astrofísica de Canarias.

The Millennium Simulation databases used in this paper and the web application providing online access to them were constructed as part of the activities of the German Astrophysical Virtual Observatory (GAVO).

O.M. is grateful for the financial support provided by the NEWFELPRO fellowship project in Croatia.

REFERENCES

Adami C., Biviano A., Mazure A., 1998, A&A, 331, 439
Adami C. et al., 2011, A&A, 526, A18
Ahn C. P. et al., 2014, ApJS, 211, 17
Baldry I. K. et al., 2014, MNRAS, 441, 2240
Benítez N., 2000, ApJ, 536, 571
Bernardi M., Hyde J. B., Sheth R. K., Miller C. J., Robert R. C., 2007, AJ, 133, 1741
Bertin E., 2011, in Evans I. N., Accomazzi A., Mink D. J., Rots A. H., eds, ASP Conf. Ser. Vol. 442, Automated Morphometry with SExtractor and PSFEx. Astron. Soc. Pac., San Francisco, p. 435
Bertin E., Arnouts S., 1996, A&AS, 117, 393
Bildfell C., Hoekstra H., Babul A., Mahdavi A., 2008, MNRAS, 389, 1637
Bîrzan L., Rafferty D. A., Nulsen P. E. J., McNamara B. R., Röttgering H. J. A., Wise M. W., Mittal R., 2012, MNRAS, 427, 3468
Biviano A., Katgert P., Thomas T., Adami C., 2002, A&A, 387, 8
Bleem L. E., Stalder B., Brodwin M., Busha M. T., Gladders M. D., High F. W., Rest A., Wechsler R. H., 2015, ApJSS, 216, 20
Bruzual G., Charlot S., 2003, MNRAS, 344, 1000
Burke C., Collins C. A., 2013, MNRAS, 434, 2856
Butcher H., Oemler A. J., 1984, ApJ, 285, 426
Chabrier G., 2003, PASP, 115, 763
Chandrasekhar S., 1943, ApJ, 97, 255
Clerc N., Pierre M., Pacaud F., Sadibekova T., 2012, MNRAS, 423, 3545
Clerc N. et al., 2014, MNRAS, 444, 2723
Collins C. A. et al., 2009, Nature, 458, 603
Conroy C., Gunn J. E., White M., 2009, ApJ, 699, 486
Coupon J. et al., 2009, A&A, 500, 981
Coupon J. et al., 2015, MNRAS, 449, 1352
Crawford C. S., Allen S. W., Ebeling H., Edge A. C., Fabian A. C., 1999, MNRAS, 306, 857
Dawson K. S. et al., 2013, AJ, 145, 10
De Lucia G., Blaizot J., 2007, MNRAS, 375, 2
De Lucia G., Springel V., White S. D. M., Croton D., Kauffmann G., 2006, MNRAS, 366, 499
Desai S. et al., 2012, ApJ, 757, 83
Donahue M., Stocke J. T., Giola I. M., 1992, ApJ, 385, 49
Dressler A. et al., 1997, ApJ, 490, 577
Edge A. C., Stewart G. C., Fabian A. C., 1992, MNRAS, 258, 177
Edwards L. O. V., Patton D. R., 2012, MNRAS, 425, 287
Edwards L. O. V., Hudson M. J., Balogh M. L., Smith R. J., 2007, MNRAS, 379, 100
Eisenstein D. J. et al., 2011, AJ, 142, 72
Elliott J., de Souza R. S., Krone-Martins A., Cameron E., Ishida E. E. O., Hilbe J., 2015, Astron.Comput., 10, 61
Fabian A. C., 2012, ARA&A, 50, 455
Flaugher B. et al., 2015, AJ, 150, 150
Garilli B. et al., 2014, A&A, 562, A23
Giles P. A. et al., 2016, A&A, 592, A3 (XXL Paper III)
Gonzales A. H., Zaritsky D., Zabuldoff A. I., 2007, ApJ, 666, 147
Gunn J. E. et al., 2006, AJ, 131, 2332
Guo F., Oh S. P., 2009, MNRAS, 400, 1992
Guzzo L. et al., 2014, A&A, 566, A108
Gwyn S. D. J., 2012, AJ, 143, 38
Haarsma D. B. et al., 2010, ApJ, 713, 1037
Henriques B. M. B., White S. D. M., Lemson G., Thomas P. A., Guo Q., Marleau G.-D., Overzier R. A., 2012, MNRAS, 421, 2904
Hopkins A. M. et al., 2012, MNRAS, 430, 2047
Hudson D. S., Mittal R., Reiprich T. H., Nulsen P. E. J., Andernach H., Sarazin C. L., 2010, A&A, 513, 37
Ilbert O. et al., 2006, A&A, 457, 841
Leauthaud A. et al., 2012, ApJ, 744, 159
Le Brun A. M. C., McCarthy I. G., Schaye J., Ponman T. J., 2014, MNRAS, 441, 1270
Le Fèvre O. et al., 2003, in Iye M., Moorwood A. F. M., eds, Proc. SPIE Conf. Ser. Vol. 4841, Instrument Design and Performance for Optical/Infrared Ground-based Telescopes. SPIE, Bellingham, p. 1670
Le Fèvre O. et al., 2005, A&A, 439, 845
Lemson G., 2006, preprint (arXiv:astro-ph/0608019)
Lemson G., Springel V., 2006, Astronomical Data Analysis Software and Systems XV, ASP Conf. Ser. Vol. 351, Cosmological Simulations in a Relational Database: Modelling and Storing Merger Trees. Astron. Soc. Pac., San Francisco
Lidman C. et al., 2012, MNRAS, 427, 550
Lidman C. et al., 2013, MNRAS, 433, 825
Lidman C. et al., 2016, Publ. Astron. Soc. Aust., 33, 1
Lieu M. et al., 2016, A&A, 592, A4 (XXL Paper IV)
Liske J. et al., 2015, MNRAS, 452, 2087
Liu F. S., Xia X. Y., Mao S., Wu H., Deng Z. G., 2008, MNRAS, 385, 23
Liu F. S., Mao S., Deng Z. G., Xia X. Y., Wen Z. L., 2009, MNRAS, 396, 2003

Liu F. S., Mao S., Meng X. M., 2012, MNRAS, 423, 422

Liu F. S. et al., 2013, ApJ, 769, 147

Liu F. S., Lei F. J., Meng X. M., Jiang D. F., 2015, MNRAS, 447, 1491

Makino J., Hut P., 1997, ApJ, 481, 83

Maraston C. et al., 2013, MNRAS, 435, 2764

McDonald M. et al., 2016, ApJ, 817, 86

McIntosh D. H., Guo Y., Hertzberg J., Katz N., Mo H. J., van den Bosch F. C., Yang X., 2008, MNRAS, 388, 1537

Menanteau F. et al., 2010, ApJS, 191, 340

Merritt D., 1984, ApJ, 276, 26

Merritt D., 1985, ApJ, 289, 18

Merten J. et al., 2015, ApJ, 806, 4

Miller L. et al., 2013, MNRAS, 429, 2858

Mohr J. J. et al., 2012, Proc. SPIE Conf. Ser. Vol. 8451, Software and Cyberinfrastructure for Astronomy II. SPIE, Bellingham

Navarro J. F., Frenk C. S., White S. D., 1997, ApJ, 490, 493

O'Dea K. P. et al., 2010, ApJ, 719, 1619

Osterbrock D. E., Ferland G. J., 2005, Astrophysics of Gaseous Nebulae and Active Galactic Nuclei. University Science Books, Herndon, VA

Pacaud F. et al., 2006, MNRAS, 372, 578

Pacaud F. et al., 2007, MNRAS, 382, 1289

Pacaud F. et al., 2016, A&A, 592, A2 (XXL Paper II)

Pierre M. et al., 2006, MNRAS, 372, 591

Pierre M. et al., 2016, A&A, 592, A1 (XXL Paper I)

Rafferty D. A., McNamara B. R., Nulsen P. E. J., 2008, ApJ, 687, 899

Raouf M., Khosroshahi H. G., Ponman T. J., Dariush A. A., Molaeinezhad A., Tavasoli S., 2014, MNRAS, 442, 1578

Reiprich T. H., Böhringer H., 2002, ApJ, 567, 716

Ricker P. M., Sarazin C. L., 2001, ApJ, 561, 621

Ruszkowski M., Springel V., 2009, ApJ, 696, 1094

Salpeter E., 1955, ApJ, 121, 161

Sanderson A. J. R., Edge A. C., Smith G. P., 2009, MNRAS, 398, 1698

Santos J. S., Rosati P., Tozzi P., Böhringer H., Ettori S., Bignamini A., 2008, A&A, 483, 35

Santos J. S., Tozzi P., Rosati P., Böhringer H., 2010, A&A, 521, 64

Saunders W. et al., 2004, Proc. SPIE Conf. Ser. Vol. 5492, Ground-based Instrumentation for Astronomy. SPIE, Bellingham, p. 389

Schombert J. M., 1987, ApJS, 64, 643

Smee S. A. et al., 2013, AJ, 146, 32

Smith G. A. et al., 2004, Proc. SPIE Conf. Ser. Vol. 5492, Ground-based Instrumentation for Astronomy. SPIE, Bellingham, p. 410

Smith G. P. et al., 2010, MNRAS, 409, 169

Smith R. J., Lucey J. R., Conroy C., 2015, MNRAS, 449, 3441

Springel V. et al., 2005, Nature, 435, 629

Stott J. P. et al., 2010, ApJ, 718, 23

Stott J. P. et al., 2012, MNRAS, 422, 2213

Thomas D. et al., 2013, MNRAS, 431, 1383

Velander M. et al., 2014, MNRAS, 437, 2111

Vulcani B. et al., 2016, ApJ, 816, 86

Webb T. M. A. et al., 2015, ApJ, 814, 96

Willis J. P. et al., 2005, MNRAS, 363, 675

Zhang Y.-Y., Andernach H., Caretta C. A., Reiprich T. H., Böhringer H., Puchwein E., Sijacki D., Girardi M., 2011, MNRAS, 526, A105

Ziparo F. et al., 2016, A&A, 592, A9 (XXL paper X)

Zwart J. T., Jarvis M. J., Deane R. P., Bonfield D. G., Knowles K., Madhanpall N., Rahmani H., Smith D. J. B., 2014, MNRAS, 439, 1459

APPENDIX A: BCG DATA

Table A1. Summary of XXL-100-GC clusters and BCGs properties. Column 1 shows the clusters unique XXL name; column 2 shows the cluster redshift. Columns 3 and 4, respectively show the mass inside of $r_{500,\,MT}$ and the value of $r_{500,\,MT}$ based on Lieu et al. 2016 $M - T$ scaling relation. BCG positions are given in columns 5 and 6; column 7 shows the BCG redshift. BCG offset from the X-ray centroid is shown in columns 8 and 9. Column 10 shows BCG stellar masses and column 11 gives the z-band magnitude difference between the brightest and second brightest cluster members.

Name	$z_{cluster}$	M_{500} 10^{13} M$_\odot$	r_{500} Mpc	BCG RA J2000	BCG Dec. J2000	z_{BCG}	BCG offset (arcsec)	r_{500}	BCG mass 10^{11} M$_\odot$	Δm_{12} z mag
(1)	(2)	(3)	(4)	(5)	(6)	(7)	(8)	(9)	(10)	(11)
XLSSC 001	0.614	25 ± 12	0.777	36.2388	-3.8147	0.617	7.6	0.067	$5.01^{+0.69}_{-0.51}$	2.19
XLSSC 003	0.836	19 ± 11	0.643	36.9092	-3.2992	0.838	1.3	0.015	$6.42^{+1.38}_{-1.06}$	0.07
XLSSC 006	0.429	41 ± 18	0.982	35.4380	-3.7674	0.429	17.4	0.100	$12.70^{+1.22}_{-1.05}$	0.10
XLSSC 010	0.330	17 ± 8	0.751	36.8432	-3.3609	0.330	3.9	0.025	$6.06^{+0.54}_{-0.37}$	1.94
XLSSC 011	0.054	17 ± 9	0.831	36.5403	-4.9682	0.050	3.4	0.004	$2.88^{+0.22}_{-0.14}$	0.81
XLSSC 022	0.293	11 ± 5	0.671	36.9181	-4.8586	0.295	3.8	0.025	$6.01^{+0.53}_{-0.35}$	0.65
XLSSC 023	0.328	11 ± 5	0.655	35.1895	-3.4333	0.328	7.5	0.054	$6.44^{+0.58}_{-0.38}$	0.61
XLSSC 025	0.265	16 ± 7	0.751	36.3530	-4.6791	0.264	1.8	0.010	$6.13^{+0.54}_{-0.34}$	1.01
XLSSC 027	0.295	17 ± 8	0.768	37.0187	-4.8499	0.294	25.8	0.149	$5.73^{+0.51}_{-0.33}$	0.22
XLSSC 029	1.050	22 ± 12	0.626	36.0174	-4.2240	1.050	3.8	0.050	$6.64^{+2.04}_{-1.49}$	2.58
XLSSC 036	0.492	24 ± 11	0.801	35.5286	-3.0540	0.496	5.4	0.041	$10.30^{+1.22}_{-0.81}$	1.05
XLSSC 041	0.142	10 ± 4	0.670	36.3782	-4.2385	0.143	1.4	0.005	$3.51^{+0.28}_{-0.18}$	1.41
XLSSC 050	0.141	23 ± 10	0.897	36.4372	-3.2091	0.142	93.0	0.258	$5.28^{+0.41}_{-0.28}$	0.37
XLSSC 054	0.053	11 ± 5	0.723	36.3185	-5.8870	0.054	3.3	0.005	$3.35^{+0.27}_{-0.16}$	0.81
XLSSC 055	0.232	21 ± 10	0.843	36.4555	-5.8962	0.233	5.9	0.026	$10.90^{+0.94}_{-0.60}$	1.04
XLSSC 056	0.348	22 ± 11	0.824	33.8676	-4.6781	0.347	18.3	0.110	$12.20^{+1.11}_{-0.75}$	0.94
XLSSC 057	0.153	13 ± 6	0.734	34.0505	-4.2394	0.154	8.2	0.030	$6.49^{+0.51}_{-0.35}$	0.63
XLSSC 060	0.139	47 ± 20	1.136	33.6712	-4.5673	0.140	54.6	0.118	$14.30^{+1.07}_{-0.79}$	0.93

Table A1 – *continued*

Name	$z_{cluster}$	M_{500} 10^{13} M$_\odot$	r_{500} Mpc	BCG RA J2000	BCG Dec. J2000	z_{BCG}	BCG offset (arcsec)	r_{500}	BCG mass 10^{11} M$_\odot$	Δm_{12} z mag
(1)	(2)	(3)	(4)	(5)	(6)	(7)	(8)	(9)	(10)	(11)
XLSSC 061	0.259	11 ± 6	0.678	35.4848	-5.7588	0.259	4.2	0.025	$8.94^{+0.79}_{-0.50}$	2.18
XLSSC 072	1.002	19 ± 11	0.613	33.8500	-3.7256	–	1.9	0.025	$5.46^{+1.61}_{-1.08}$	0.58
XLSSC 083	0.430	37 ± 20	0.943	32.7350	-6.1985	0.429	4.8	0.030	$6.40^{+0.64}_{-0.51}$	0.01
XLSSC 084	0.430	36 ± 25	0.945	32.7621	-6.2130	0.432	18.6	0.119	$3.02^{+0.30}_{-0.24}$	0.15
XLSSC 085	0.428	41 ± 27	0.976	32.8697	-6.1963	0.429	2.9	0.018	$10.30^{+1.03}_{-0.81}$	1.03
XLSSC 087	0.141	8 ± 3	0.619	37.7208	-4.3478	0.141	3.4	0.014	$4.87^{+0.38}_{-0.26}$	1.04
XLSSC 090	0.141	4 ± 2	0.507	37.1222	-4.8565	0.142	4.4	0.022	$4.74^{+0.37}_{-0.25}$	2.42
XLSSC 091	0.186	51 ± 22	1.149	37.9215	-4.8825	0.185	17.2	0.047	$9.32^{+0.76}_{-0.51}$	0.49
XLSSC 093	0.429	23 ± 11	0.810	31.7002	-6.9471	0.429	6.0	0.042	$6.30^{+0.62}_{-0.51}$	0.00
XLSSC 096	0.520	48 ± 31	1.000	30.9709	-5.0279	0.521	6.9	0.043	$6.93^{+0.86}_{-0.56}$	1.05
XLSSC 097	0.760	32 ± 19	0.794	33.3426	-6.0990	0.695	4.3	0.041	$7.48^{+1.37}_{-1.00}$	0.06
XLSSC 098	0.297	20 ± 12	0.801	33.1144	-6.0751	0.296	5.3	0.034	$7.26^{+0.64}_{-0.42}$	1.13
XLSSC 099	0.391	46 ± 40	1.032	33.2196	-6.2033	0.361	5.7	0.029	$8.07^{+0.77}_{-0.57}$	1.49
XLSSC 100	0.915	26 ± 18	0.694	31.5473	-6.1920	0.915	6.0	0.069	$6.27^{+1.57}_{-1.07}$	0.62
XLSSC 101	0.756	31 ± 16	0.788	32.1957	-4.4310	0.753	21.0	0.198	$13.40^{+2.40}_{-1.79}$	1.80
XLSSC 103	0.233	27 ± 17	0.913	36.8866	-5.9644	0.232	13.7	0.056	$6.42^{+0.56}_{-0.35}$	0.08
XLSSC 104	0.294	–	1.038	37.3287	-5.8872	0.291	31.6	0.135	$6.75^{+0.59}_{-0.39}$	0.12
XLSSC 105	0.429	47 ± 24	1.024	38.4158	-5.5109	0.452	23.3	0.129	$4.82^{+0.48}_{-0.38}$	0.18
XLSSC 106	0.300	24 ± 11	0.856	31.3676	-5.7324	0.302	61.1	0.320	$8.10^{+0.72}_{-0.47}$	0.40
XLSSC 107	0.436	16 ± 8	0.711	31.3541	-7.5945	0.439	2.1	0.017	$5.48^{+0.55}_{-0.45}$	0.35
XLSSC 108	0.254	13 ± 6	0.705	31.8335	-4.8252	0.255	8.9	0.051	$7.15^{+0.63}_{-0.40}$	1.41
XLSSC 109	0.491	23 ± 15	0.787	32.2967	-6.3453	0.487	3.0	0.023	$8.37^{+0.96}_{-0.68}$	0.32
XLSSC 111	0.299	40 ± 18	1.017	33.1124	-5.6265	0.300	5.0	0.022	$11.50^{+1.05}_{-0.64}$	0.57
XLSSC 112	0.139	9 ± 4	0.653	32.5093	-5.4678	0.138	24.5	0.093	$5.35^{+0.41}_{-0.29}$	0.92
XLSSC 113	0.050	5 ± 2	0.560	30.5610	-7.0082	0.051	1.7	0.003	$3.34^{+0.26}_{-0.17}$	0.19
XLSSC 114	0.234	44 ± 51	1.070	30.4207	-5.0302	–	16.8	0.059	$9.19^{+0.81}_{-0.50}$	1.15
XLSSC 115	0.043	12 ± 7	0.740	32.6798	-6.5797	0.043	30.3	0.035	$2.84^{+0.22}_{-0.14}$	0.46
XLSSC 502	0.141	5 ± 2	0.532	348.4413	-53.4368	0.140	5.0	0.023	$6.29^{+0.48}_{-0.33}$	1.47
XLSSC 503	0.336	10 ± 5	0.642	350.6469	-52.7470	0.334	3.8	0.029	$5.70^{+0.51}_{-0.34}$	0.26
XLSSC 505	0.055	9 ± 4	0.661	352.2513	-52.2364	0.055	6.7	0.011	$8.27^{+0.65}_{-0.40}$	0.76
XLSSC 507	0.566	12 ± 6	0.612	353.3732	-52.2537	0.569	7.4	0.080	$8.18^{+1.07}_{-0.67}$	0.12
XLSSC 509	0.633	29 ± 17	0.806	356.4538	-54.0466	0.635	26.7	0.230	$4.50^{+0.61}_{-0.49}$	0.02
XLSSC 510	0.395	15 ± 7	0.711	357.5395	-55.3331	0.395	2.3	0.018	$5.29^{+0.50}_{-0.37}$	1.59
XLSSC 511	0.130	5 ± 2	0.545	357.7522	-55.3704	0.133	3.7	0.016	$2.77^{+0.21}_{-0.14}$	0.38
XLSSC 512	0.402	26 ± 12	0.848	352.4831	-56.1357	0.402	2.3	0.014	$9.51^{+0.90}_{-0.69}$	1.00
XLSSC 513	0.378	34 ± 17	0.936	349.2161	-54.8990	0.377	21.7	0.121	$11.10^{+1.05}_{-0.70}$	0.45
XLSSC 514	0.169	7 ± 3	0.582	351.3990	-54.7208	0.169	12.0	0.060	$4.30^{+0.34}_{-0.23}$	0.55
XLSSC 515	0.101	5 ± 2	0.540	351.4173	-54.7419	0.100	6.7	0.023	$5.62^{+0.43}_{-0.28}$	1.03
XLSSC 517	0.699	20 ± 12	0.698	350.4494	-55.9704	0.697	1.1	0.012	$6.34^{+0.90}_{-0.83}$	0.12
XLSSC 518	0.177	5 ± 2	0.535	349.8214	-55.3243	0.177	3.9	0.022	$7.71^{+0.61}_{-0.42}$	0.87
XLSSC 519	0.270	6 ± 3	0.555	353.0194	-55.2123	0.270	2.3	0.017	$4.99^{+0.43}_{-0.28}$	0.92
XLSSC 520	0.175	17 ± 7	0.805	352.5017	-54.6188	0.176	0.8	0.003	$11.00^{+0.82}_{-0.64}$	2.10
XLSSC 521	0.807	31 ± 18	0.775	352.1791	-55.5669	0.807	0.4	0.004	$13.70^{+2.74}_{-2.13}$	0.84
XLSSC 522	0.395	15 ± 7	0.711	351.6401	-55.0199	0.395	10.3	0.078	$5.62^{+0.53}_{-0.40}$	0.28
XLSSC 523	0.343	19 ± 10	0.779	350.5019	-54.7499	0.345	3.0	0.019	$4.76^{+0.42}_{-0.29}$	0.21

Table A1 – *continued*

Name	$z_{cluster}$	M_{500} 10^{13} M$_\odot$	r_{500} Mpc	BCG RA J2000	BCG Dec. J2000	z_{BCG}	BCG offset (arcsec)	r_{500}	BCG mass 10^{11} M$_\odot$	Δm_{12} z mag
(1)	(2)	(3)	(4)	(5)	(6)	(7)	(8)	(9)	(10)	(11)
XLSSC 524	0.270	16 ± 8	0.754	353.0646	− 54.7032	0.269	11.4	0.063	$6.30^{+0.54}_{-0.35}$	0.28
XLSSC 525	0.379	24 ± 10	0.832	349.3403	− 53.9612	0.371	6.9	0.044	$9.22^{+0.85}_{-0.61}$	0.45
XLSSC 527	0.076	24 ± 27	0.926	349.5734	− 55.9839	0.076	13.3	0.021	$6.47^{+0.51}_{-0.31}$	0.41
XLSSC 528	0.302	23 ± 12	0.839	349.6818	− 56.2034	0.303	3.2	0.017	$9.91^{+0.86}_{-0.57}$	0.69
XLSSC 529	0.547	23 ± 11	0.769	349.7037	− 56.2865	0.548	15.6	0.131	$6.38^{+0.82}_{-0.51}$	0.62
XLSSC 530	0.182	11 ± 5	0.686	348.8342	− 54.3440	0.190	5.7	0.026	$6.04^{+0.48}_{-0.33}$	0.29
XLSSC 531	0.391	38 ± 30	0.966	349.8752	− 56.6495	0.390	3.6	0.020	$10.00^{+0.98}_{-0.66}$	0.24
XLSSC 532	0.392	19 ± 10	0.772	352.9477	− 52.6657	0.391	11.0	0.077	$5.69^{+0.54}_{-0.40}$	0.32
XLSSC 533	0.107	15 ± 6	0.789	351.7243	− 52.6971	0.108	46.0	0.115	$4.60^{+0.35}_{-0.23}$	0.04
XLSSC 534	0.853	27 ± 18	0.725	350.1089	− 53.3587	0.853	12.5	0.131	$6.57^{+1.44}_{-1.11}$	0.43
XLSSC 535	0.172	14 ± 6	0.756	351.5538	− 53.3162	0.171	1.7	0.006	$9.30^{+0.73}_{-0.51}$	0.51
XLSSC 537	0.515	39 ± 21	0.934	354.0297	− 53.8766	0.517	3.4	0.023	$13.00^{+1.56}_{-1.03}$	1.86
XLSSC 538	0.332	20 ± 12	0.804	354.6477	− 54.6242	0.332	6.8	0.041	$9.88^{+0.87}_{-0.59}$	0.41
XLSSC 539	0.184	5 ± 2	0.520	355.7959	− 55.8814	0.182	5.4	0.030	$7.26^{+0.59}_{-0.39}$	0.78
XLSSC 540	0.414	20 ± 9	0.776	355.6308	− 56.3532	0.411	4.9	0.035	$9.01^{+0.86}_{-0.68}$	0.86
XLSSC 541	0.188	18 ± 8	0.805	355.4330	− 55.9637	0.188	8.2	0.032	$5.54^{+0.45}_{-0.29}$	0.51
XLSSC 542	0.402	74 ± 32	1.202	353.1145	− 53.9744	0.405	8.7	0.039	$14.40^{+1.37}_{-1.04}$	0.97
XLSSC 543	0.381	14 ± 7	0.689	354.8637	− 55.8407	0.383	10.1	0.077	$5.70^{+0.53}_{-0.38}$	0.33
XLSSC 544	0.095	15 ± 7	0.788	349.8155	− 53.5330	0.096	2.7	0.006	$8.17^{+0.63}_{-0.40}$	0.17
XLSSC 546	0.792	20 ± 10	0.668	352.4201	− 53.2489	0.860	13.6	0.154	$4.51^{+0.87}_{-0.67}$	0.30
XLSSC 547	0.371	32 ± 18	0.920	351.4277	− 53.2768	0.370	2.1	0.010	$11.60^{+1.05}_{-0.74}$	0.98
XLSSC 550	0.109	3 ± 2	0.480	352.2079	− 52.5770	0.107	8.5	0.035	$5.34^{+0.41}_{-0.27}$	1.42

[1] *Department of Physics and Astronomy, University of Victoria, 3800 Finnerty Road, Victoria, BC V8P 1A1, Canada*
[2] *Service d'Astrophysique AIM, CEA Saclay, F-91191 Gif sur Yvette, France*
[3] *Department of Astronomy, University of Geneva, ch. d'Écogia 16, CH-1290 Versoix, Switzerland*
[4] *INAF, IASF Milano, via Bassini 15, I-20133 Milano, Italy*
[5] *School of Physics and Astronomy, University of Birmingham, Birmingham B152TT, UK*
[6] *Australian Astronomical Observatory, PO Box 915, North Ryde 1670, Australia*
[7] *Université Aix-Marseille, CNRS, LAM (Laboratoire d'Astrophysique de Marseille) UMR 7326, F-13388 Marseille, France*
[8] *Argelander-Institut für Astronomie, University of Bonn, Auf dem Hügel 71, D-53121 Bonn, Germany*
[9] *Max-Planck-Institut für extraterrestrische Physik, Giessenbach- straße, D-85748 Garching, Germany*
[10] *H.H. Wills Physics Laboratory, University of Bristol, Tyndall Avenue, Bristol BS8 1TL, UK*
[11] *ESA, Villafranca del Castillo, Spain*
[12] *Department of Astronomy, University of Florida, Gainesville, FL 32611, USA*
[13] *Astrophysics Research Institute, Liverpool John Moores University, IC2, Liverpool Science Park, 146 Brownlow Hill, Liverpool L3 5RF, UK*
[14] *INAF – Observatory of Rome, via Frascati 33, I-00040 Monteporzio Catone, Rome, Italy*

[15] *Faculty of Physics, Ludwig Maximilian Universität, München, Germany*
[16] *Dipartimento di Fisica e Astronomia, Universita' di Bologna, Viale Berti Pichat 6/2, I-40127 Bologna, Italy*
[17] *Main Astronomical Observatory, Academy of Sciences of Ukraine, 27 Akademika Zabolotnoho St., UA-03680 Kyiv, Ukraine*
[18] *Department of Physics and Astronomy, Macquarie University, Sydney, NSW 2109, Australia*
[19] *Max-Planck Institut fuer Kernphysik, Saupfercheckweg 1, D-69117 Heidelberg, Germany*
[20] *Institut d'Astrophysique Spatiale (IAS), bat. 121, F-91405 Orsay Cedex, France*
[21] *INAF, Osservatorio Astronomico di Brera, Merate, Italy*
[22] *Universität Hamburg, Hamburger Sternwarte, Gojenbergsweg 112, D-21029 Hamburg, Germany*
[23] *Department of Physics, University of Zagreb, Bijenicka cesta 32, HR-10000 Zagreb, Croatia*
[24] *Astronomical Observatory, Taras Shevchenko National University of Kyiv, Observatorna str. 3, UA-04053 Kyiv, Ukraine*
[25] *INAF, Osservatorio Astronomico di Padova, Vicolo dell'Osservatorio, 5, I-35122 Padova, Italy*

This paper has been typeset from a TeX/LaTeX file prepared by the author.